論　文　題　目

Seasonal Variation of Circulations in the East China Sea and the Yellow Sea

（東シナ海と黄海における循環流の季節変動）

氏　　名

Satoru TAKAHASHI
（高橋　暁）

１９９４年

①

論 文 題 目

Seasonal Variation of Circulations in the East China Sea and the Yellow Sea

（東シナ海と黄海における循環流の季節変動）

氏　名

Satoru TAKAHASHI
（高 橋　暁）

１９９４年

学位論文要旨

化石燃料の大量消費にともない大気中の二酸化炭素濃度は急激に増加しており、このことが地球上の気候や生態系に大きな影響を与えるのではないかと懸念されている。このため、大気中の二酸化炭素の変動特性を明らかにし、対策を立てることが急務となっている。

現在、化石燃料の消費によって放出された二酸化炭素の約半分が大気中に残留しているが、残り半分の吸収の場として海洋が最も有力視されており、生物生産性は低いが面積的に大きな部分を占める外洋域での研究が進められている。しかしながら、海洋微生物による無機炭素の利用や河川からの物質供給等を考えると、面積的に占める割合は小さいが、生物生産性が高く、人為的な影響を直接受け、外洋へとつながっている縁辺海，陸棚海域における炭素の循環メカニズムを明らかにすることは非常に重要である。

縁辺海，陸棚海域における炭素の循環メカニズムを考える上で、その海域の物質輸送や無機炭素を取り込む海洋微生物の分布を把握することが重要であるが、このような問題に対して、海域の流況が与える影響は大きい。そこで、本研究では黄河，揚子江の二大河川が流入し、生物生産性の非常に高い黄海・東シナ海を対象海域として、先ず診断モデルを用いて流況の季節変動を定量的に明らかにし、次に、得られた結果中の顕著な流動現象について、その力学機構を明らかにすることを試みた。

１章では、上述したような本研究の目的について述べた。

２章では、現実的な地形を持った診断モデルを使って、東シナ海・黄海の流況の季節変動を定量的に明らかにすることを試みた。その結果、夏には、黄海中央部の上層に反時計回りの循環流が、下層では逆に時計回りの循環流が形成された。これは、夏に黄海中央部の下層に見られる黄海底部冷水にともなう流れであると考えられる。冬には、黄海中央部に上層から下層までの全層を通して時計回りの循環流が形成された。また、東シナ海北部に全層を通して反時計回りの循環流が形成された。反時計回りの循環流は、密度分布を与えず、冬の風応力のみを強制力として与えた場合においても形成された。つまり、この循環流は、冬の北西の季節風によって引き起こされていると考えられる。また、春と秋の結果は両者ともほぼ冬の結果と同じパターンであった。

３章では、２種類の円形のモデル地形を持ち、外力として海面加熱を与えた数値モデル実験によって、２章でその存在が示唆された夏の黄海における上層で反時計回りの、下層で時計回りの循環流の形成機構を調べた。地形性貯熱効果によって形成される密度分布が励起する鉛直循環流によって海域中央部の上層では水平収束となり、下層では水平発散となる。この水平の収束と発散にともなって、海域中央部上層には正の、下層には負の渦度が発生し、上層と下層にそれぞれ反時計回りと時計回りの循環流が形成されることが確かめられた。一方、鉛直の水温分布は、潮流

による鉛直かき混ぜ効果の水平的な違いによる影響を受けていることが明らかとなった。この水温分布によって表層で時計回りの循環流が形成されたが、その強さは地形性貯熱効果によるものに比べ非常に弱いため、表層の反時計回りの循環流を弱める程度に留まった。現実の夏の黄海の水平循環流と水温分布は、これら地形性貯熱効果と潮流による鉛直かき混ぜ効果が重なり合って形成されていると考えられる。

4章では、2章でその存在が示唆された冬の黄海における循環流の形成と維持の機構を、簡単化された黄海の地形と水深を持ち、強制力として風応力を与えた数値モデルを用いて調べた。北西からの一様な風によって中国東岸沖に反時計回り、韓国西岸沖に時計回りの2つの渦が形成された。これら2つの渦は双方とも陸棚波として岸を右に見て伝播する。反時計回りの渦は風応力とバランスできず発達しなかったが、時計回りの渦は風応力とバランスして、黄海北部で発達し、約2日後に平衡に達した。また、4日周期の変動を持った北西風によって励起される時計回りの渦は風の変動にともなって周期的に励起・伝播を繰り返すことが確かめられた。この変動する流動場を風の1周期で時間平均して得られた流れのパターンは、一様な風を平衡に達するまで吹かせて得られた流れのパターンとほぼ同じであった。つまり、冬の黄海の流動場には変動場と定常場が同時に存在していると考えられる。

5章では、本研究で得られた結論をまとめた。

CONTENTS

1. Introduction

Today, the carbon dioxide content in the atmosphere is becoming to one of the most important problems, because it affects the global warming. It is thus necessary to promote the study of material cycling of carbon and other elements in the sea water and the study of gas exchange at the air–sea interface and at the sea–sediments interface. Marginal seas in the Western Pacific such as the East China Sea and the Yellow Sea are regions of high biological productivity, because amount of nutrients are supplied by water discharge from rivers such as Changjiang (Yangtze) River and Huanghe (Yellow) River, and they are expected to play an important role on the material cycling in the global ocean. It could be said that if the material transport in the marginal sea is not revealed correctly, the material cycling in the global ocean is not able to be wholly understood. So, we choose the East China Sea and the Yellow Sea as one of representative marginal seas, and will investigate the water circulations in this marginal sea in this paper.

The East China Sea and the Yellow Sea are one of the most developed continental shelf areas in the world. Seasonal variation of water circulations in the East China Sea and the Yellow Sea is expected to be very large because their water depth is so shallow that the large seasonal variations in the heat transfer through the sea surface and in wind may affect the water circulations there.

As for the seasonal variation of the water circulations in the East China Sea and the Yellow Sea, the schematic figure (Niino and Emery, 1961) shown in Fig.1 is well known. But we should say that this flow pattern is not reliable even from a qualitative viewpoint, which will be discussed in section 2. The water circulation patterns in summer and winter were also given by Kondo (1985), based on the mean distribution of water properties at 50m depth, although they were only qualitative results.

Due to the difficulty of the field observation, the direct current measurements in the East China Sea and the Yellow Sea have been very few. Consequently, the seasonal variation of the water circulations in the East China Sea and the Yellow Sea has not been discussed quantitatively. We have to clarify quantitatively the seasonal variation of the water circulations in the East China Sea and the Yellow Sea in order to discuss the quantitative material transport in this marginal

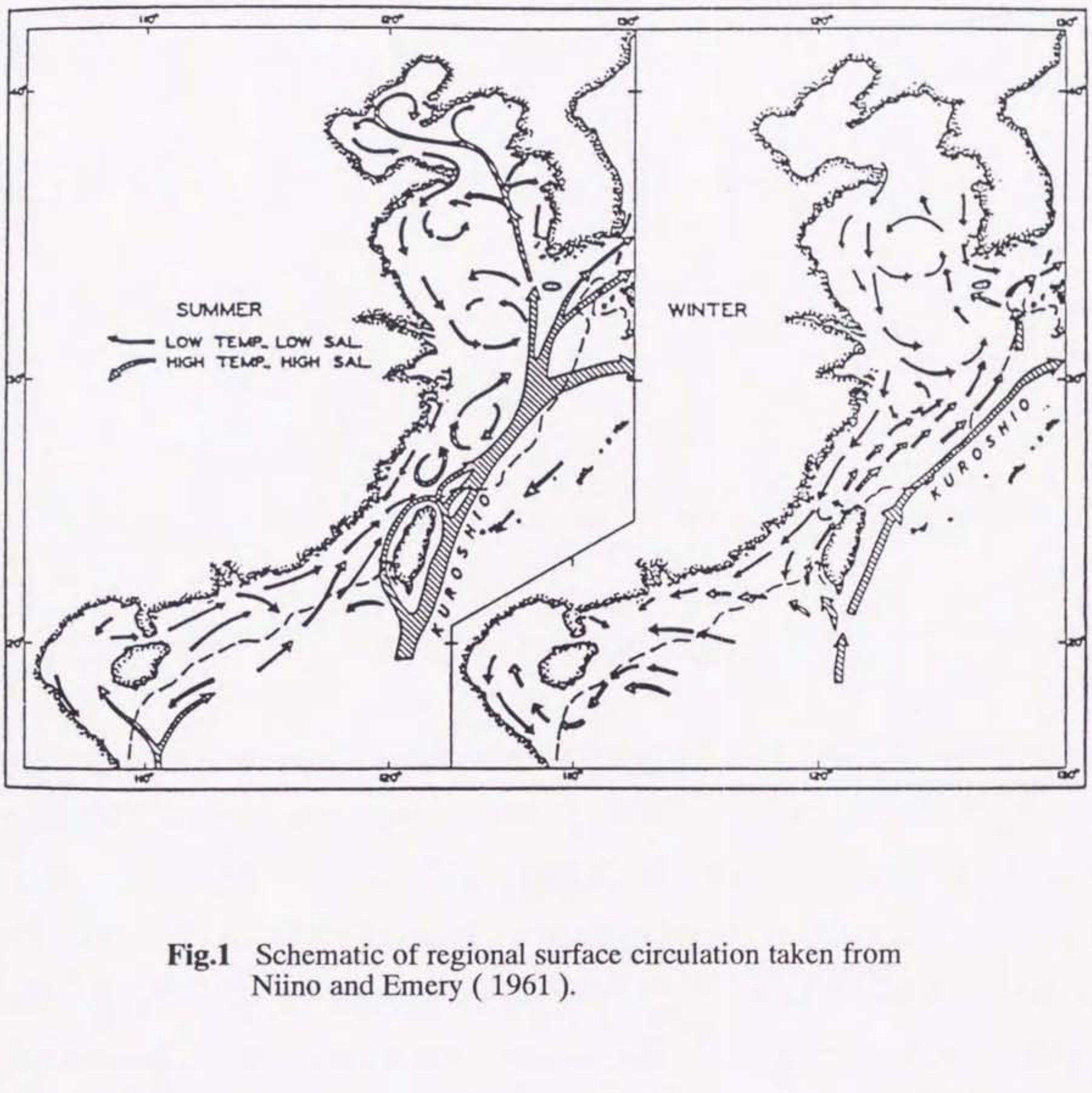

Fig.1 Schematic of regional surface circulation taken from Niino and Emery (1961).

sea. With this purpose in mind, we try to reveal the seasonal variation of the water circulations in the East China Sea and the Yellow Sea with use of a robust diagnostic three-dimensional numerical model. Furthermore, the detailed dynamical process for the remarkable circulations in the Yellow Sea will be also investigated using a prognostic numerical model.

2. Seasonal Variation of Circulations

2.1 Numerical Model

The model area is shown in Fig.2. The maximum depth in this model is 300 m due to the computational economical viewpoint. The horizontal grid size is 50 km x 50 km and the water column is vertically divided into three layers (upper: 0 – 20 m, middle: 20 – 60 m, lower: 60 m – bottom). Using conventional notation, the governing equations on the Cartesian coordinate are as follows:

$$\frac{\partial u}{\partial t} + \left(u \frac{\partial u}{\partial x} + v \frac{\partial u}{\partial y} + w \frac{\partial u}{\partial z} \right) - fv = - \frac{1}{\rho_0} \frac{\partial p}{\partial x} + A_h \left(\frac{\partial^2 u}{\partial x^2} + \frac{\partial^2 u}{\partial y^2} \right) + A_v \frac{\partial^2 u}{\partial z^2}, \quad (2\text{–}1)$$

$$\frac{\partial v}{\partial t} + \left(u \frac{\partial v}{\partial x} + v \frac{\partial v}{\partial y} + w \frac{\partial v}{\partial z} \right) + fu = - \frac{1}{\rho_0} \frac{\partial p}{\partial y} + A_h \left(\frac{\partial^2 v}{\partial x^2} + \frac{\partial^2 v}{\partial y^2} \right) + A_v \frac{\partial^2 v}{\partial z^2}, \quad (2\text{–}2)$$

$$\frac{\partial p}{\partial z} = - \rho g, \quad (2\text{–}3)$$

$$\frac{\partial u}{\partial x} + \frac{\partial v}{\partial y} + \frac{\partial w}{\partial z} = 0, \quad (2\text{–}4)$$

$$\frac{\partial T}{\partial t} + \left(u \frac{\partial T}{\partial x} + v \frac{\partial T}{\partial y} + w \frac{\partial T}{\partial z} \right) = K_h \left(\frac{\partial^2 T}{\partial x^2} + \frac{\partial^2 T}{\partial y^2} \right) + K_v \frac{\partial^2 T}{\partial z^2} + \gamma (T^* - T), \quad (2\text{–}5)$$

$$\frac{\partial S}{\partial t} + \left(u \frac{\partial S}{\partial x} + v \frac{\partial S}{\partial y} + w \frac{\partial S}{\partial z} \right) = K_h \left(\frac{\partial^2 S}{\partial x^2} + \frac{\partial^2 S}{\partial y^2} \right) + K_v \frac{\partial^2 S}{\partial z^2} + \gamma (S^* - S) \quad (2\text{–}6)$$

where u, v and w are the velocity component of x, y and z directions, respectively, f is Coriolis parameter ($2\omega\sin\varphi$, ω is angular velocity of earth rotation and φ is latitude changing from 24°40'N to 40°10'N), t is time, p is pressure, ρ is density, ρ_0 is the reference density, g is the gravitational acceleration (980 cm sec^{-2}), A_h (10^7 cm^2 sec^{-1}) and K_h (10^7 cm^2 sec^{-1}) are horizontal eddy viscosity and diffusivity, respectively, A_v (5 cm^2 sec^{-1}) and K_v (5 cm^2 sec^{-1}) are vertical eddy viscosity and diffusivity, respectively, T is water temperature, and S is salinity. The density is calculated from T and S with use of the usual nonlinear state equation (Wadachi, 1987).

The last terms in Eqs.(2–5) and (2–6) are called ρ terms which are introduced by Sarmiento

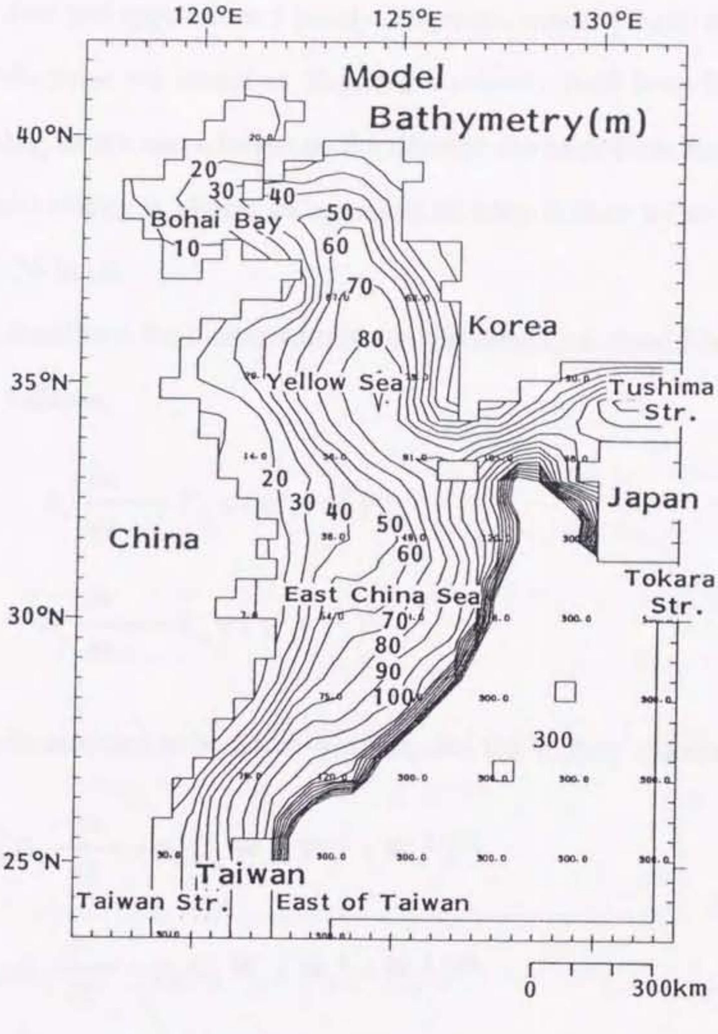

Fig.2 Model basin of the East China Sea and the Yellow Sea.
Numbers show the depth in meter.

and Bryan (1982) to prevent calculated values T and S from deviating greatly from observed values T^* and S^*. In other words, if there is an observed density that significantly deviates from a local advective-diffusive balance, the density is smoothed by the model to satisfy the balance to some extent. The degree of modification is represented by ρ. For a small ρ, the model is near to be independent of the data and approaches prognostic models. For a large ρ, the model is restricted by the data and approaches a purely diagnostic model (Fujio and Imasato, 1991). We prefer a larger ρ because we intend to diagnose a velocity field from hydrographic data, not to predict it. As long as we use a larger ρ, the density deviates little from the observed values. Hence the derived velocity is almost independent of eddy diffusivity as discussed later. In this case, we use ρ=1/24 hours.

The boundary condition for momentum is no-slip condition at the lateral walls. The bottom stress is given as follows,

$$A_v \frac{\partial u}{\partial z} = C_b\, u\, (u^2 + v^2)^{1/2} , \tag{2-7}$$

$$A_v \frac{\partial v}{\partial z} = C_b\, v\, (u^2 + v^2)^{1/2} . \tag{2-8}$$

The sea surface is assumed to be a free-surface, and the surface momentum flux is given by

$$\rho_0 A_v \frac{\partial u}{\partial z} = \rho_a C_d W_x (W_x^{\,2} + W_y^{\,2})^{1/2} , \tag{2-9}$$

$$\rho_0 A_v \frac{\partial v}{\partial z} = \rho_a C_d W_y (W_x^{\,2} + W_y^{\,2})^{1/2} \tag{2-10}$$

where C_b (0.0026) is the bottom drag coefficient, ρ_a (0.0012 g cm^{-3}) the air density, C_d (0.0013) the sea surface drag coefficient, W_x and Wy are x and y components of the wind vector, respectively. The boundary condition for water temperature and salinity is a no-flux condition at the lateral walls, at the bottom, and at the sea surface.

The effect of momentum of Kuroshio to the water circulation in this marginal sea is not considered in this model, that is, the model is closed and the volume transport of Kuroshio is not included.

The leap–frog scheme with use of Dufort–Frankel method is adopted for the temporal acceleration term, viscosity term and diffusive term and the Euler–Backward scheme is inserted every ten time steps. The central difference scheme is adopted for the advection term and the semi-implicit scheme is used for the calculation of water elevation (Backhaus, 1983).

2.2 Observed Data

The observed data of water temperature and salinity in four seasons are obtained from the Marine Environmental Atlas (Japan Oceanographic Data Center, 1978). The data of 0 m and 50 m are averaged ones from 1930 to 1970. Water temperature and salinity at three levels (10 m, 40 m, the middle depth of the lower layer) in the model are interpolated or extrapolated from observed data at 0 m and 50 m.

Wind data are obtained from COADS (Comprehensive Ocean–Atmosphere Data Set, Woodruff et al., 1987). They are averaged data every month from 1854 till 1979 at every 2 ° mesh size. The averaged wind vector in four seasons (Spring: April to June, Summer: July to September, Autumn: October to November, Winter: January to March) are calculated and those at each mesh points of this model are interpolated from the calculated data. The results are shown in Fig.3. The strong southward wind prevails in autumn and winter but the weak northward wind in spring and summer.

We examined the steadiness of density field at this marginal sea in four seasons, that is, we compare the temporal change terms of water temperature and salinity with other terms in Eqs.(2–5) and (2–6) with use of observed JODC data. As for water temperature and salinity, maximum temporal change terms in four seasons have the order of 10^{-6} °C sec^{-1} and 10^{-7} psu sec^{-1}, respectively. On the other hand, the advective and diffusive terms of water temperature and salinity have the order of 10^{-5} °C sec^{-1} and 10^{-6} psu sec^{-1}, respectively, using the values of $u = 3$ cm sec^{-1} and $K_h = 10^7$ cm^2 sec^{-1}. Therefore, we may consider that the density and flow fields at this marginal sea in four seasons are quasi–steady state.

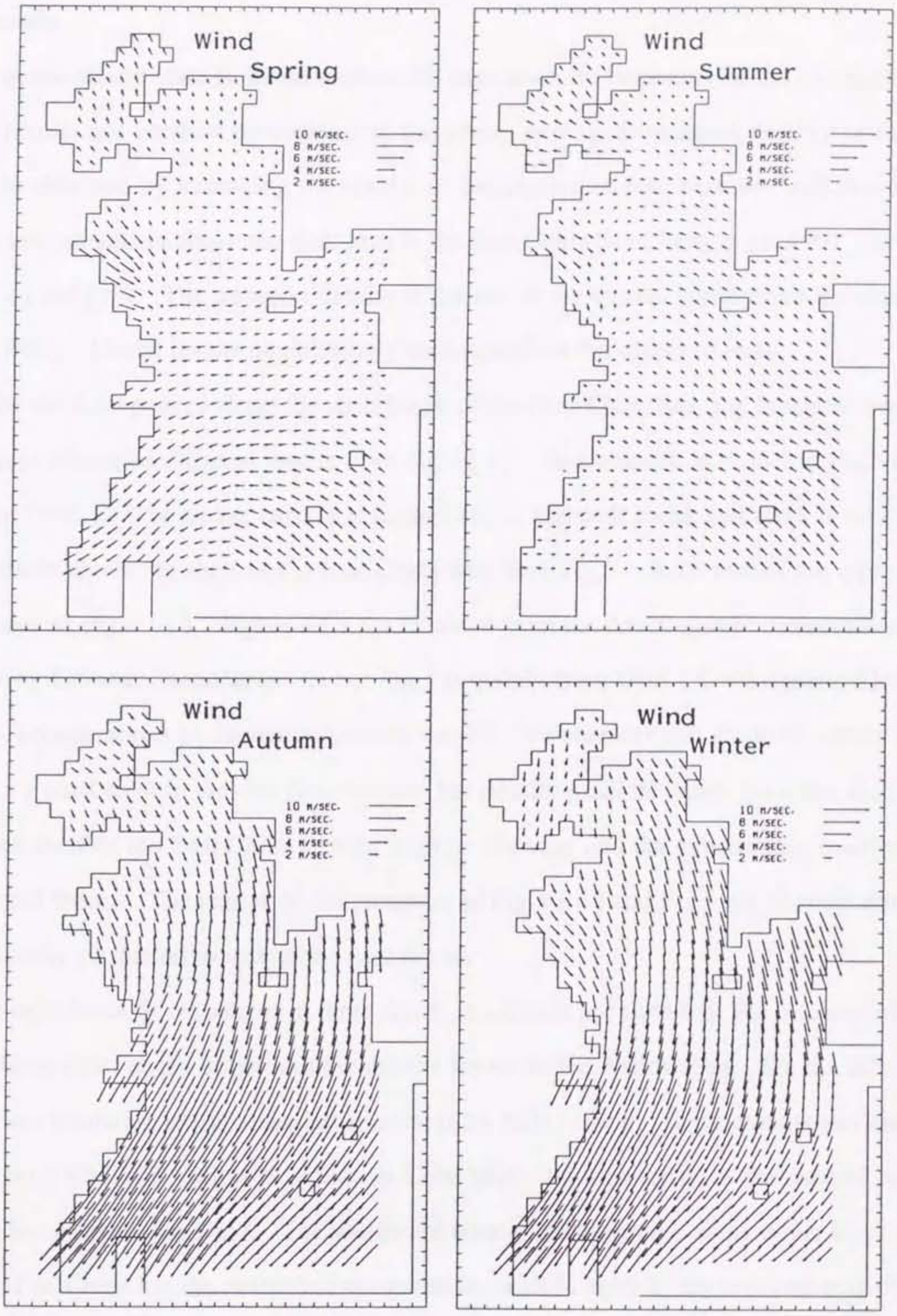

Fig.3 Seasonal variation in wind vector from COADS.

2.3 Results

The quasi–steady state is obtained about 20 days after the beginning of the calculation. The model results are verified by comparing the yearly averaged transport density in the model, which is obtained by averaging the results of calculation in four seasons, and that from 566 current measurements above the shelf area in the East China Sea (Fang et al., 1991) as shown in Fig.4 (a) and (b). The transport density is defined as the current speed times the depth (Fang et al., 1991). Model results quantitatively well reproduce the observed ones.

As for the flow pattern along the shelf break of the East China Sea, the Japanese oceanographers have presented different results from Fig.4 (a). One example is shown in Fig.5 (Qiu and Imasato, 1990). The strong current is limited above the shelf break and there is no systematic flow pattern above the shelf in the East China Sea from Fig.5. Such results are quite different from those of Fig.4 (a). Figure 4 (a) is obtained from the direct current measurements at 566 stations by Chinese Oceanographers but Fig.5 is mainly from GEK (Geomagnetic Electrokinetograph) observations by Japanese research vessels. We consider that the flow pattern shown in Fig.4 (a) must exist in the real field because the density gradient exists from the shelf break to the inner shelf of the East China Sea throughout the year and the geostrophic relation may be established there. The reason of disagreement of Fig.4 (a) and Fig.5 are obscure now and we have to study on this difference in the near future.

The calculated flow patterns at three layers in summer are shown in Fig.6. Anti–clockwise circulations exist at the upper and the middle layers in the Yellow Sea. On the other hand, a clockwise circulation exists at the lower layer in the Yellow Sea. These circulations are accompanied by YSBCW (Yellow Sea Bottom Cold Water) which exists at the central part of the Yellow Sea as shown in Fig.7. The southward coastal current exists at the upper layer along the mainland of China but the northward current at the middle layer in the northern part of the East China Sea.

Figure 8 shows the result of drifter buoys tracking during July to October, 1986 (Choi and Lie, 1992) and the tracks of buoys in the Yellow Sea well coincide with the result of the upper

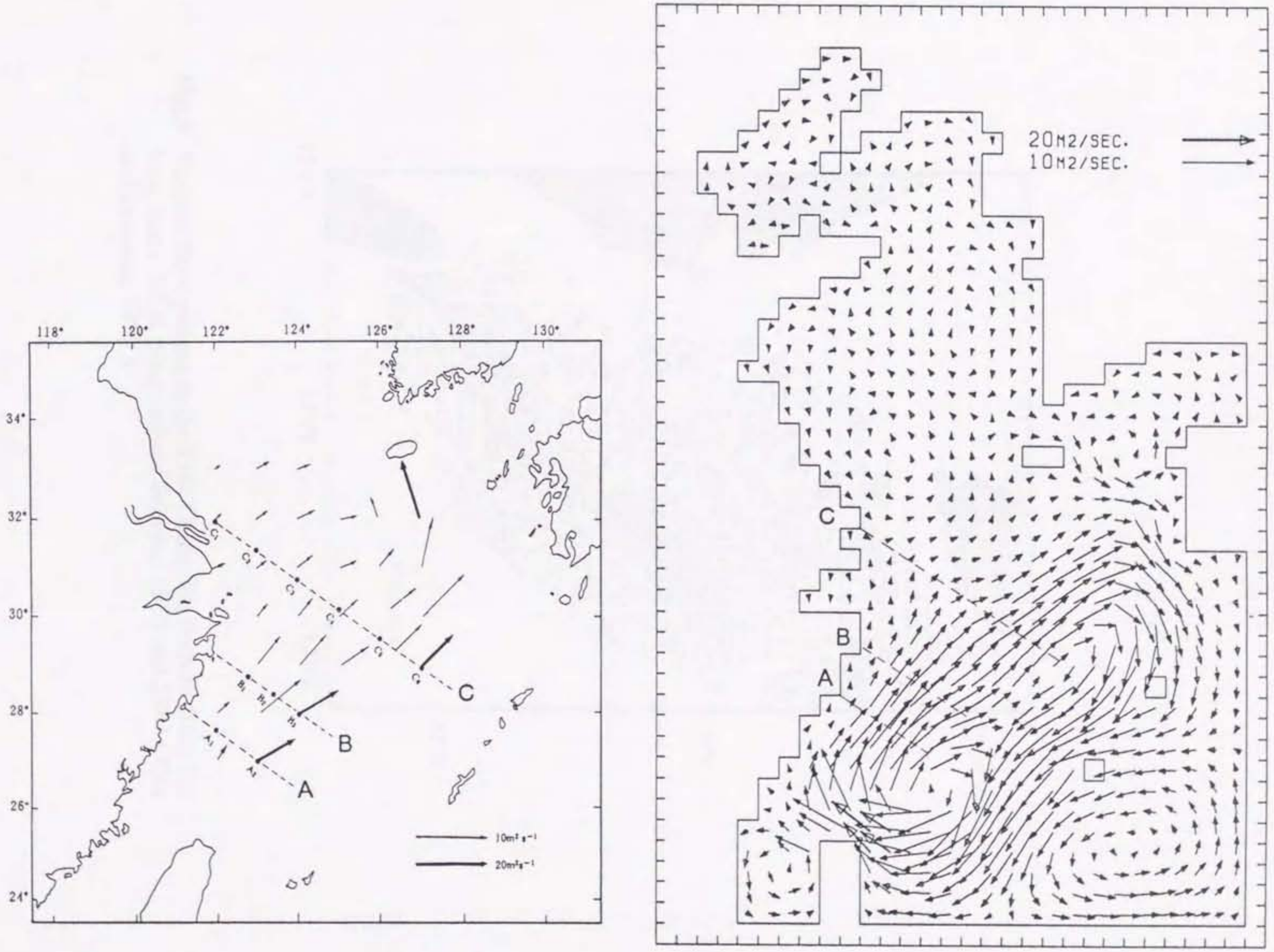

Fig.4 Observed averaged transport density (current speed times the depth) by Fang et al. (1991) (a) and calculated yearly-averaged one in the model (b).

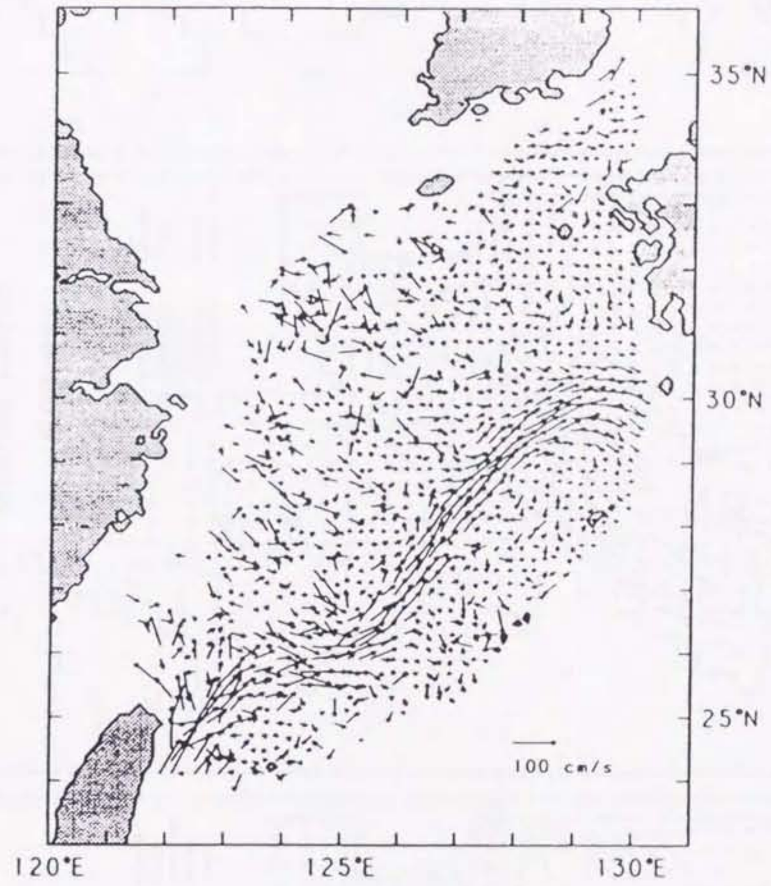

Fig.5 Surface flow pattern in the East China Sea derived from the long term GEK observations between 1953 and 1984 (Qiu and Imasato, 1990).

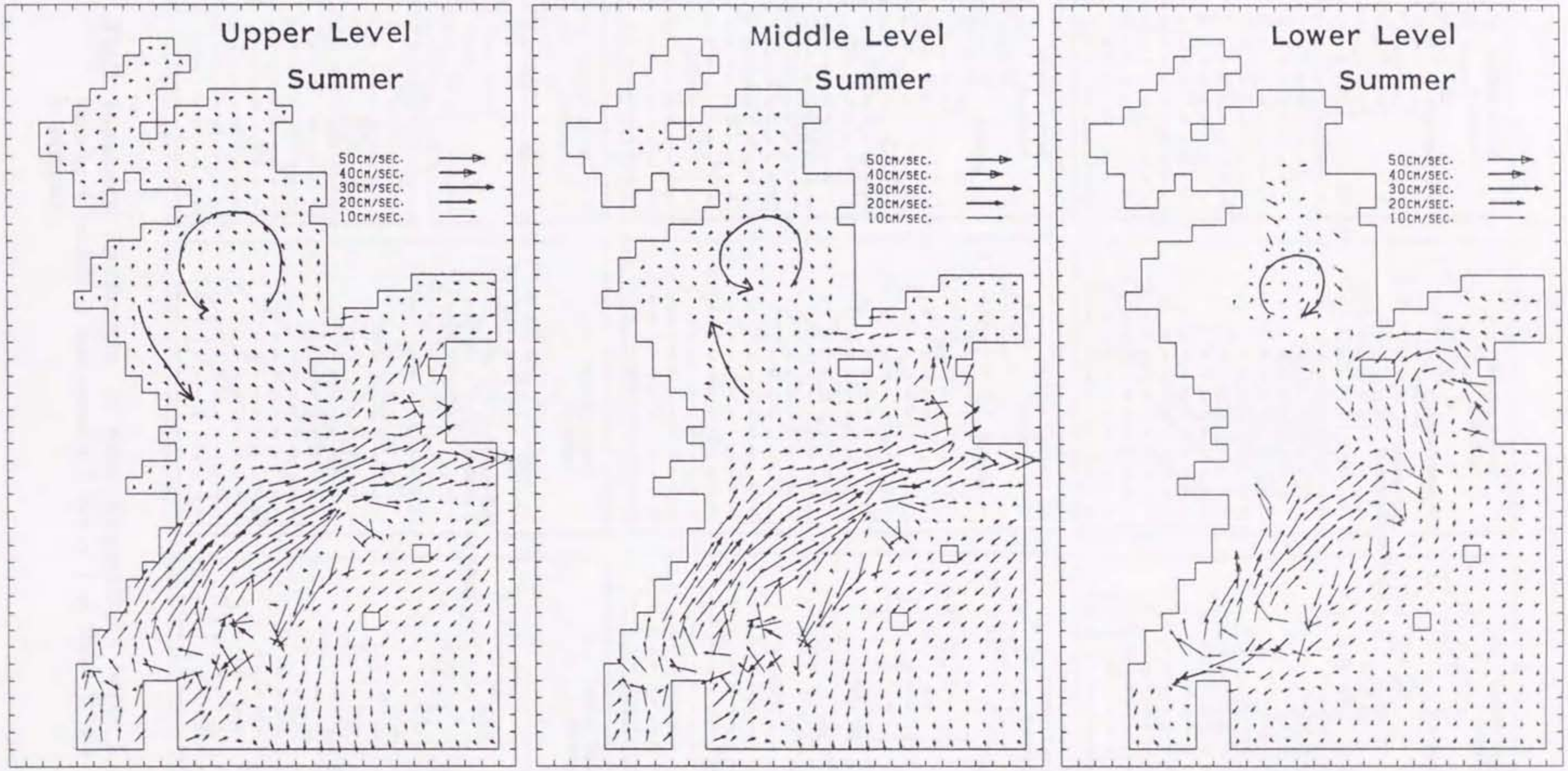

Fig.6 Current distributions at three levels in summer.

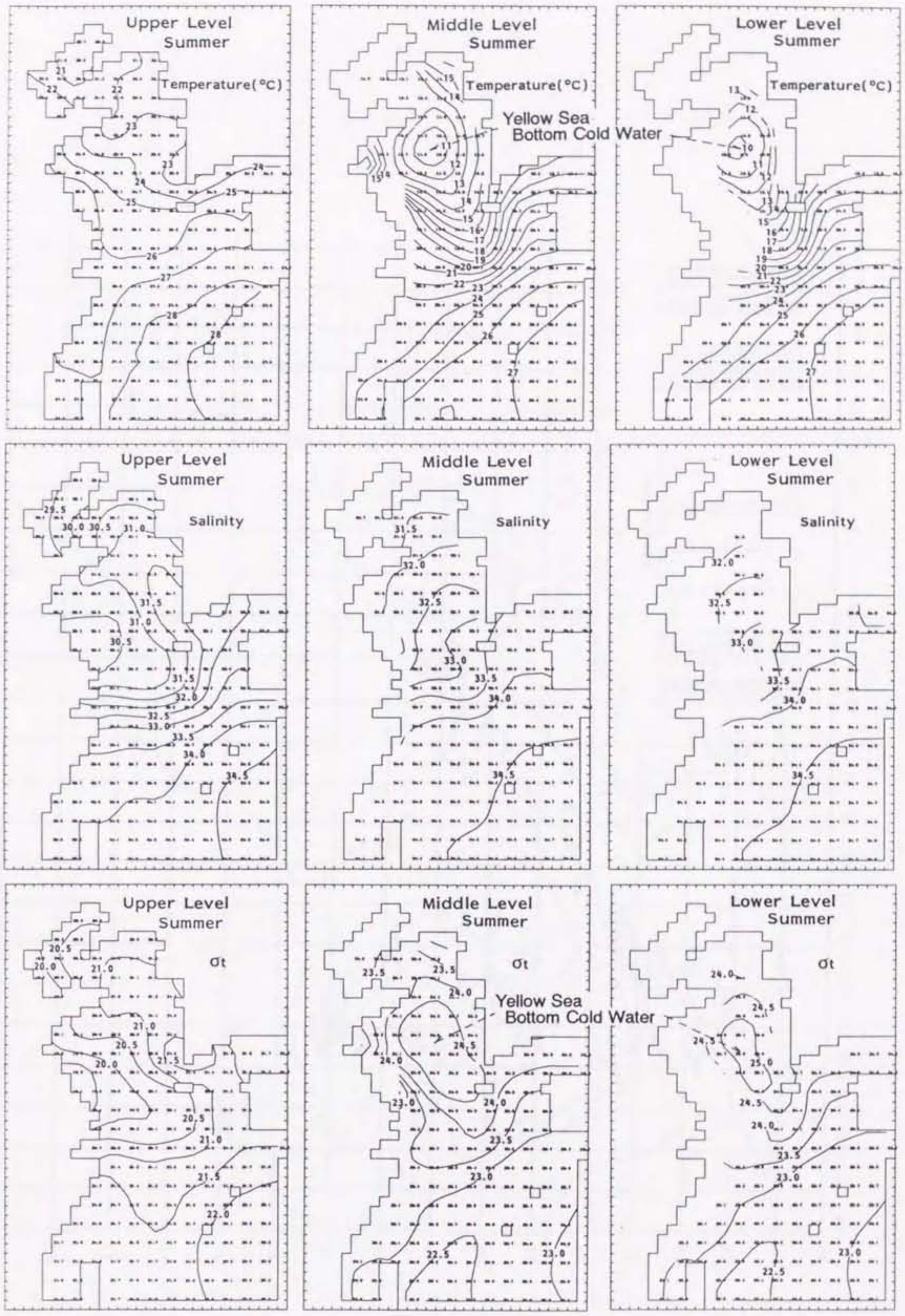

Fig.7 Horizontal distributions of water temperature (upper), salinity (middle) and density (lower) at three levels in summer.

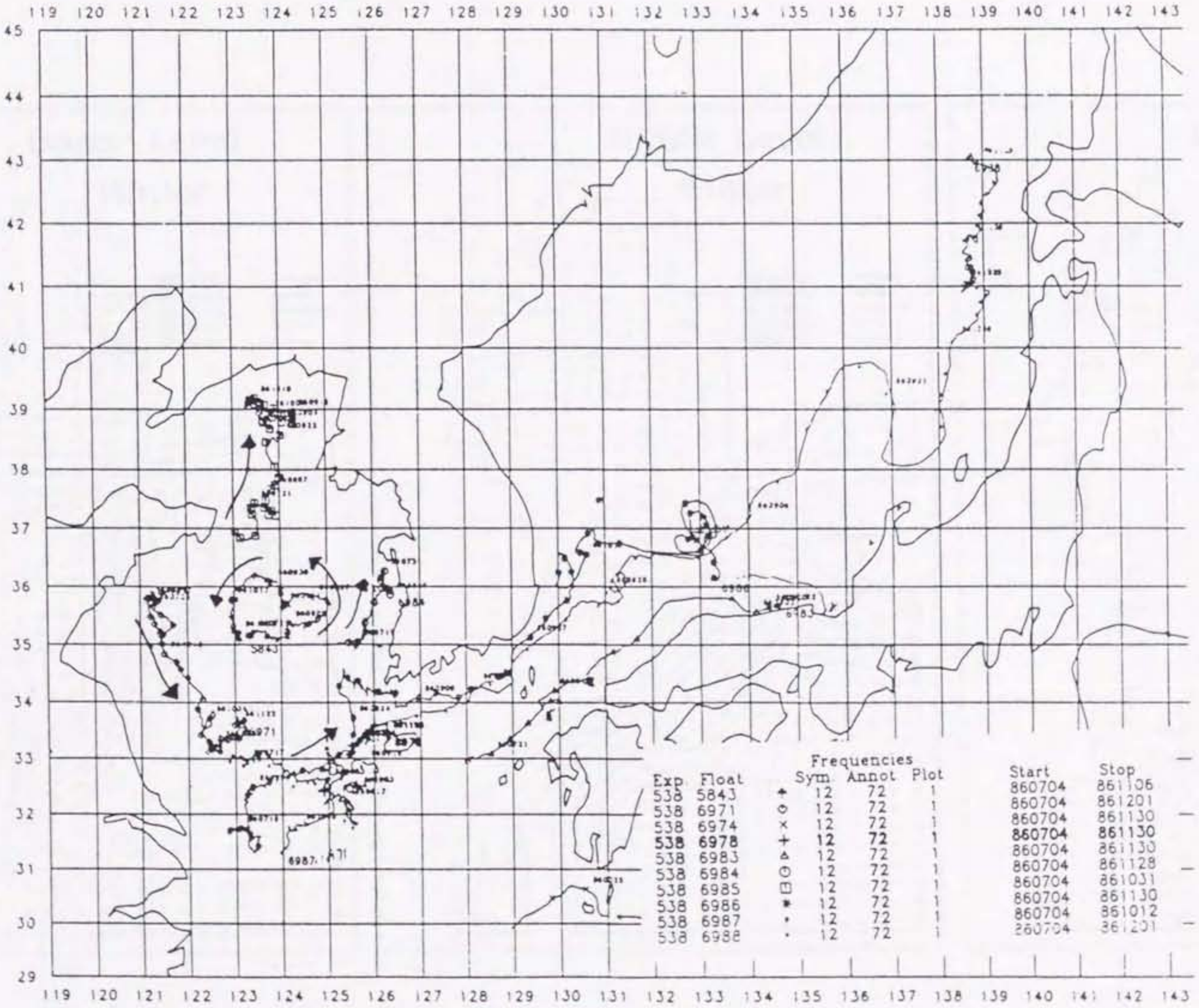

Exp	Float	Sym	Frequencies Sym	Annot	Plot	Start	Stop
538	5843	♠	12	72	1	860704	861106
538	6971	○	12	72	1	860704	861201
538	6974	×	12	72	1	860704	861130
538	6978	+	12	72	1	860704	861130
538	6983	△	12	72	1	860704	861130
538	6984	⊙	12	72	1	860704	861128
538	6985	⊟	12	72	1	860704	861031
538	6986	✱	12	72	1	860704	861130
538	6987	•	12	72	1	860704	861012
538	6988	·	12	72	1	860704	861201

Fig.8 Track of ARGOS satellite drifter buoys during July to October, 1986 (Choi and Lie (1992).

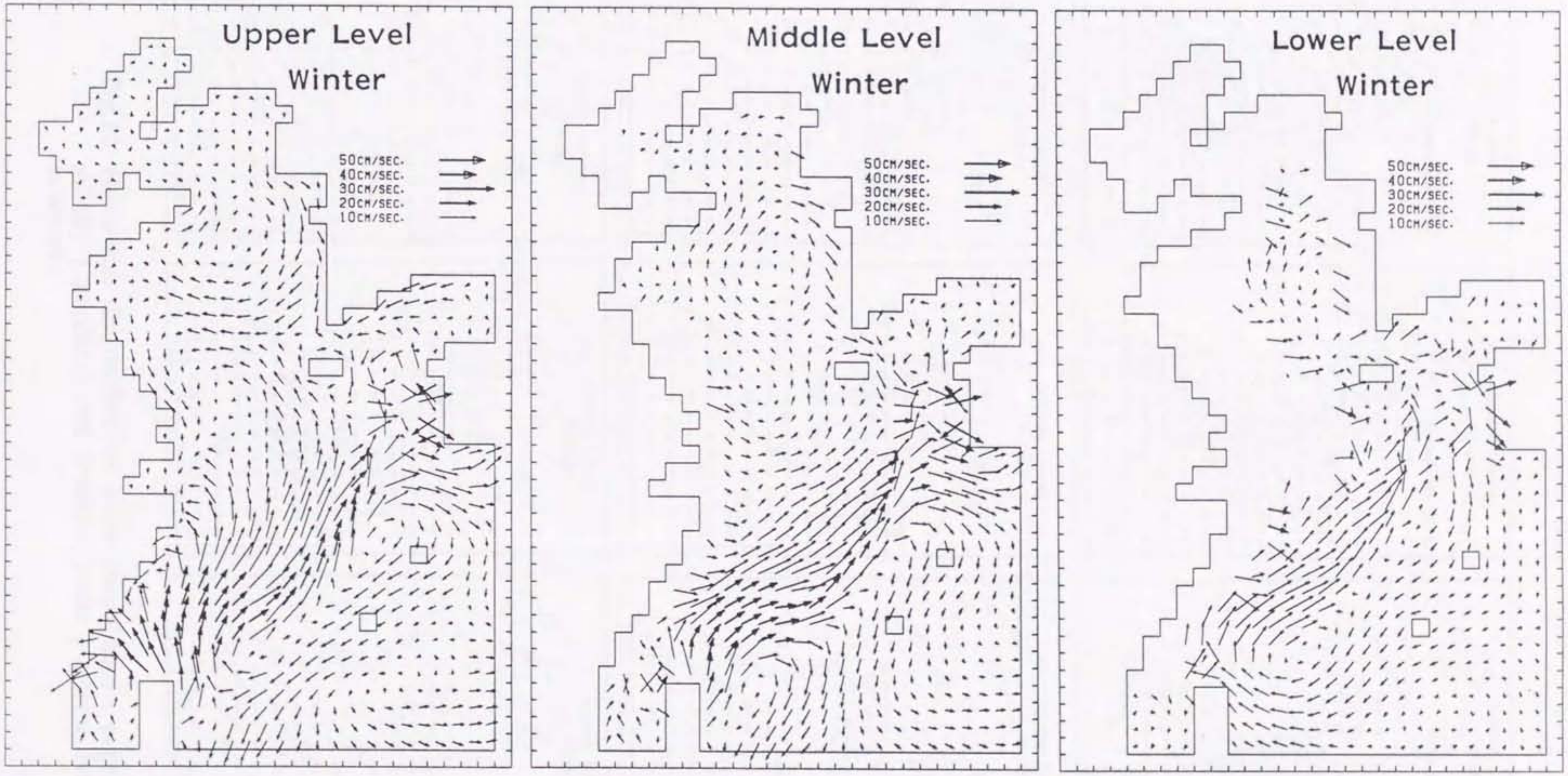

Fig.9 Current distributions at three levels in winter.

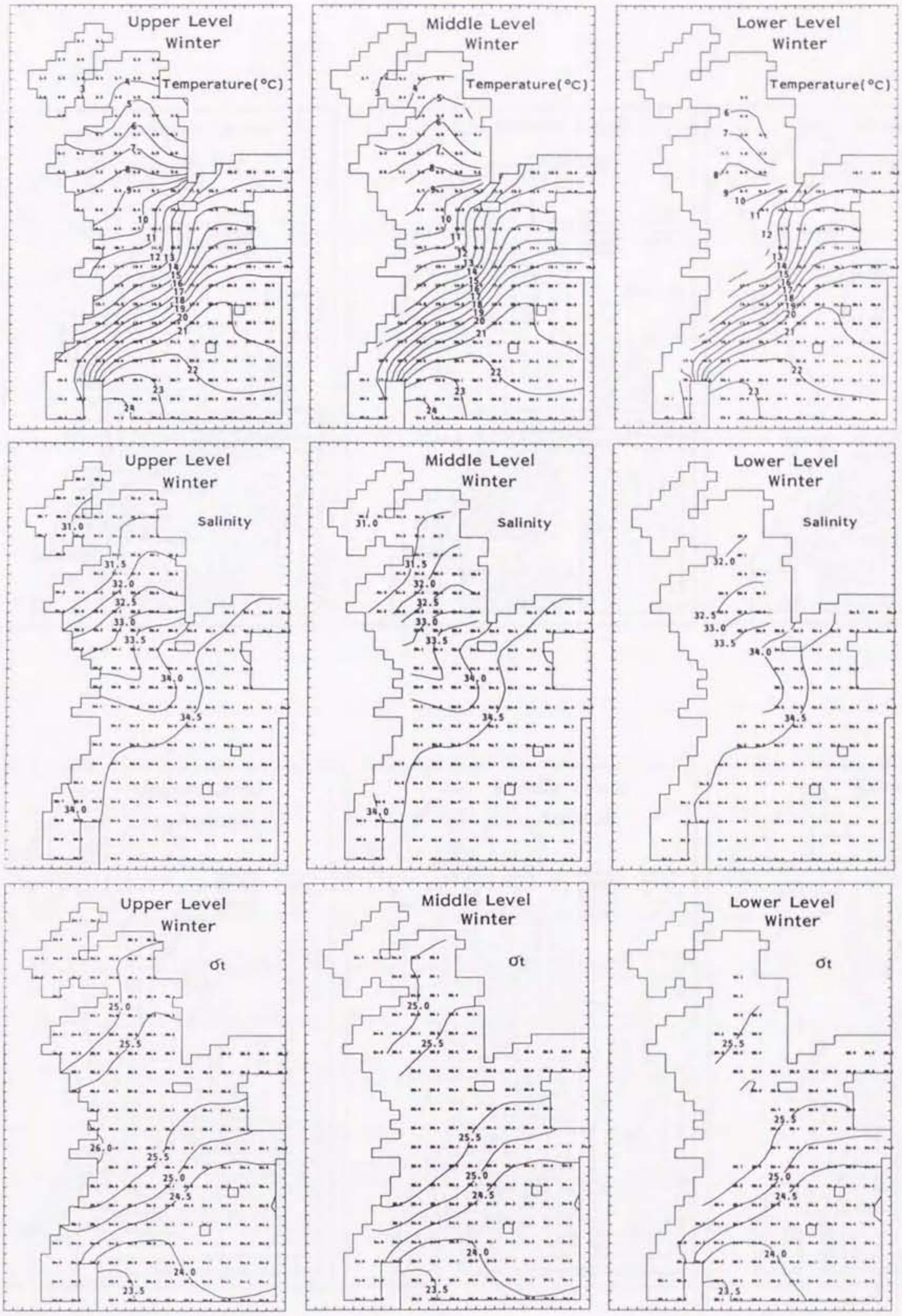

Fig.10 Horizontal distributions of water temperature (upper), salinity (middle) and density (lower) at three levels in winter.

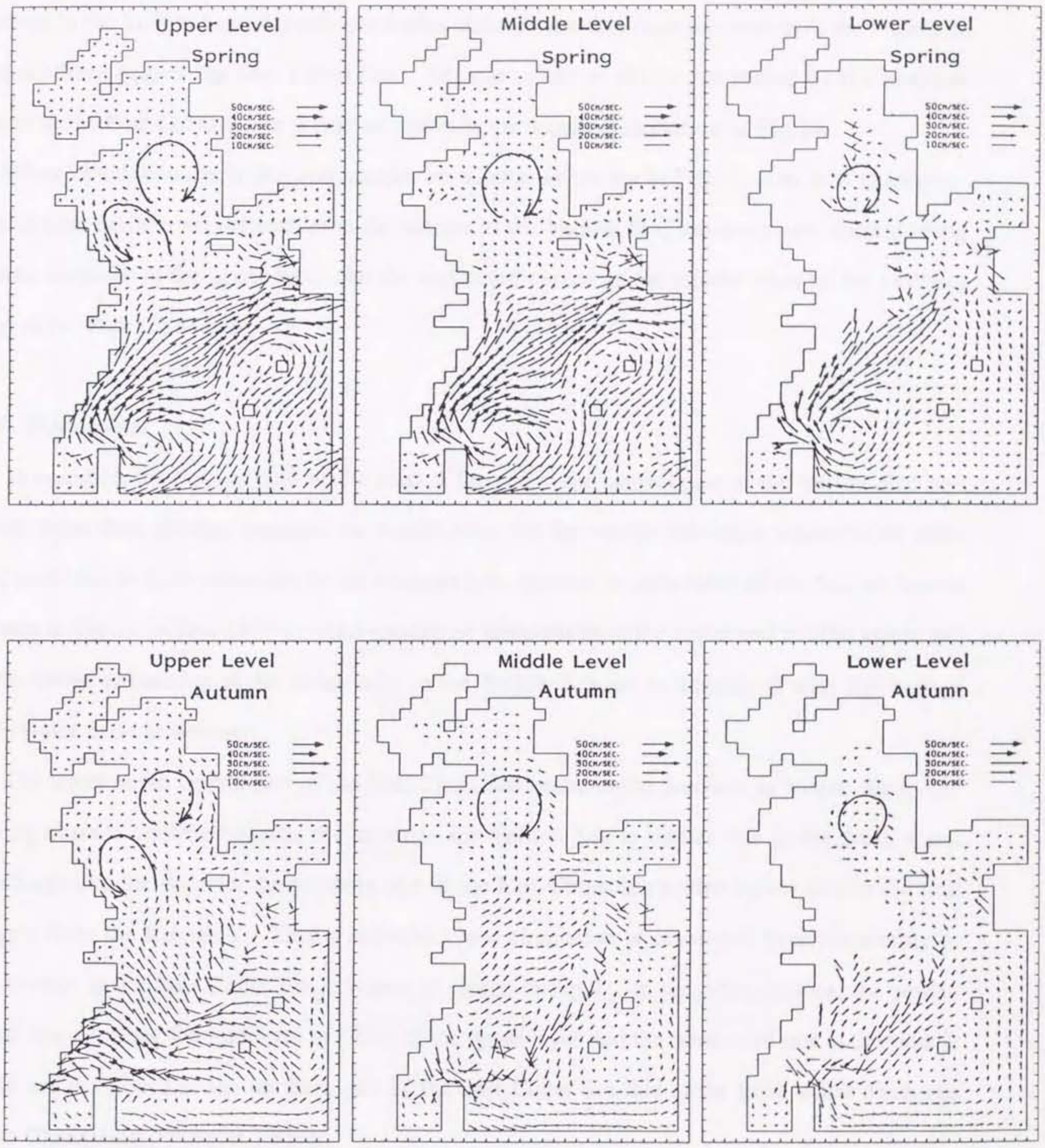

Fig.11 Water circulations in spring (upper) and in autumn (lower).

layer of Fig.6 qualitatively.

The results in winter are shown in Fig.9. A clockwise circulation exists from the surface to the bottom in the Yellow Sea. An anti-clockwise circulation exists from the surface to the bottom in the northern part of the East China Sea. Such circulations are accompanied by the heaviest water in the East China Sea in winter as shown in the density distribution of Fig.10.

Water circulations in spring and autumn are similar as shown in Fig.11 , that is, a clockwise circulation exists from the surface to the bottom in the Yellow Sea, the southward current along China develops at the upper layer and the northward current at the middle layer in the northern part of the East China Sea.

2.4 Discussions

In summer, the bottom cold water mass is formed at the central part of the Yellow Sea because the surface heating generates the stratification but the vertical mixing is weaker in the central part than in both sides due to the stronger tidal current in both sides of the Yellow Sea as shown in Fig.12 (Choi, 1979). Anti-clockwise circulations at the upper and middle layers and a clockwise circulation at the lower layer in the Yellow Sea are accompanied with this bottom cold water mass in summer.

The water at the central part of the East China Sea becomes the heaviest in winter due to the strong surface cooling because the water in the Yellow Sea is lighter due to the fresh water discharge and the water in the southern part of the East China Sea is also lighter due to the heat supply from the Kuroshio. Then a anti-clockwise circulation is developed from the surface to the bottom in the East China Sea in winter as shown in Fig.8. In the other seasons, the southward current along the mainland of China at the upper layer and the northward one at the middle layer are developed in the northern part of the East China Sea due to the fresh water discharge from Changjiang (Yangtze) River.

The direct wind effect to the water circulations in this marginal sea is examined in summer and in winter and the model results without density distribution (barotropic motion) are shown in Figs.13 and 14. There is no dominant circulation in summer due to weak wind stress in

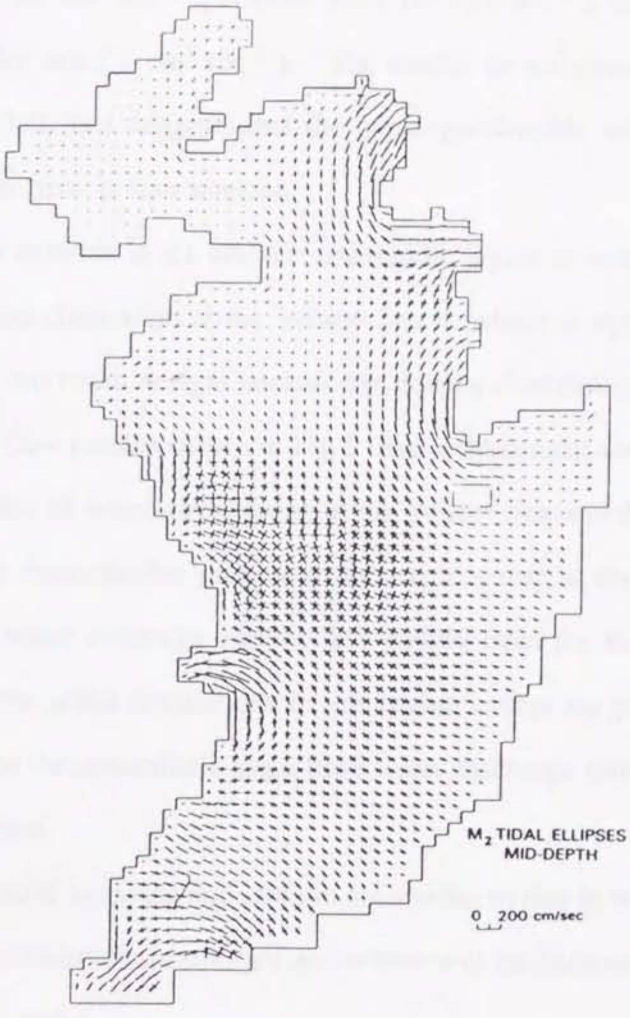

Fig.12 Computed tide-induced residual flow and principal axes of the M_2 tidal current ellipses at mid depth (Choi, 1984).

summer as shown in Fig.13. On the other hand, a remarkable clockwise circulation develops at the Yellow Sea in winter as shown in Fig.14. Such fact suggests that the clockwise circulation at the Yellow Sea in winter is mainly due to the strong wind and bottom topography.

We also examined the effect of viscosity and carried out the numerical computations with larger horizontal viscosity (10^8 cm^2 sec^{-1}), smaller one (10^6 cm^2 sec^{-1}), larger vertical viscosity (10 cm^2 sec^{-1}) and smaller one (1 cm^2 sec^{-1}). The results do not remarkably change from those mentioned above. Such fact suggests that the quasi-geostrophic relation is established in the East China and Yellow Seas in four seasons.

The calculated flow patterns in the surface and middle layers in summer are similar to that of Fig.1 but the calculated circulation at the Yellow Sea in winter is opposite to the circulation of Fig.1. We think that our result is right because the density distribution in winter shown in Fig.9 cannot balance to the flow pattern shown in Fig.1 from a dynamical viewpoint.

The seasonal variation of water circulations in the Yellow Sea and the East China Sea may be highly affected by the thermohaline process in this region, that is, the heat transfer through the sea surface, the fresh water discharge and the heat supply from the Kuroshio mainly govern the seasonal variation of the water circulations in this region except the periods when the abnormal strong wind blowing or the anomalistic large fresh water discharge drastically change the density distribution in this region.

Since water circulations in spring and autumn are similar to that in winter, the detailed dynamical process of water circulations in summer and winter will be discussed with use of the numerical model in sections 3 and 4.

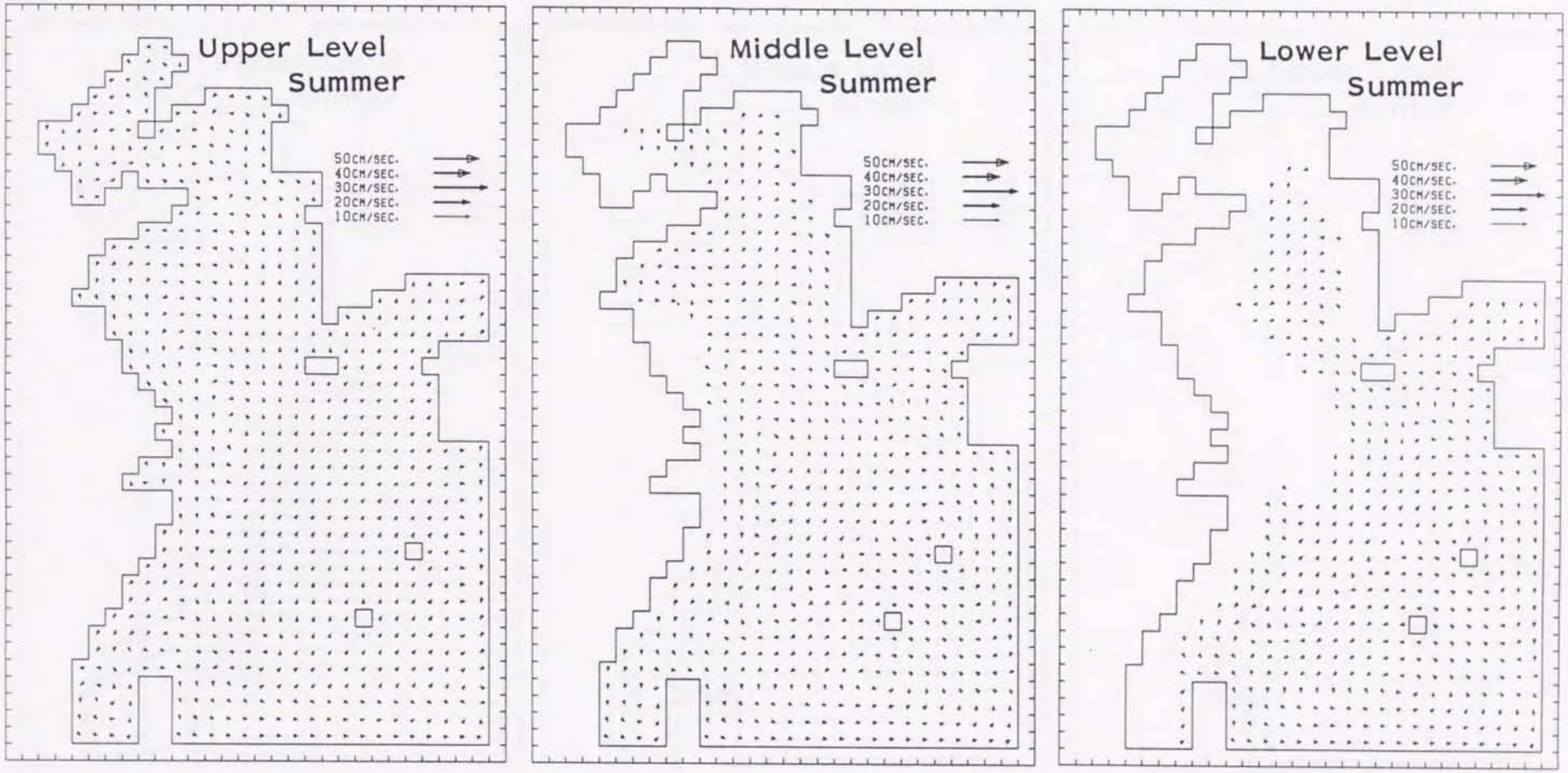

Fig.13 Water circulations in summer with wind stress and without density distribution.

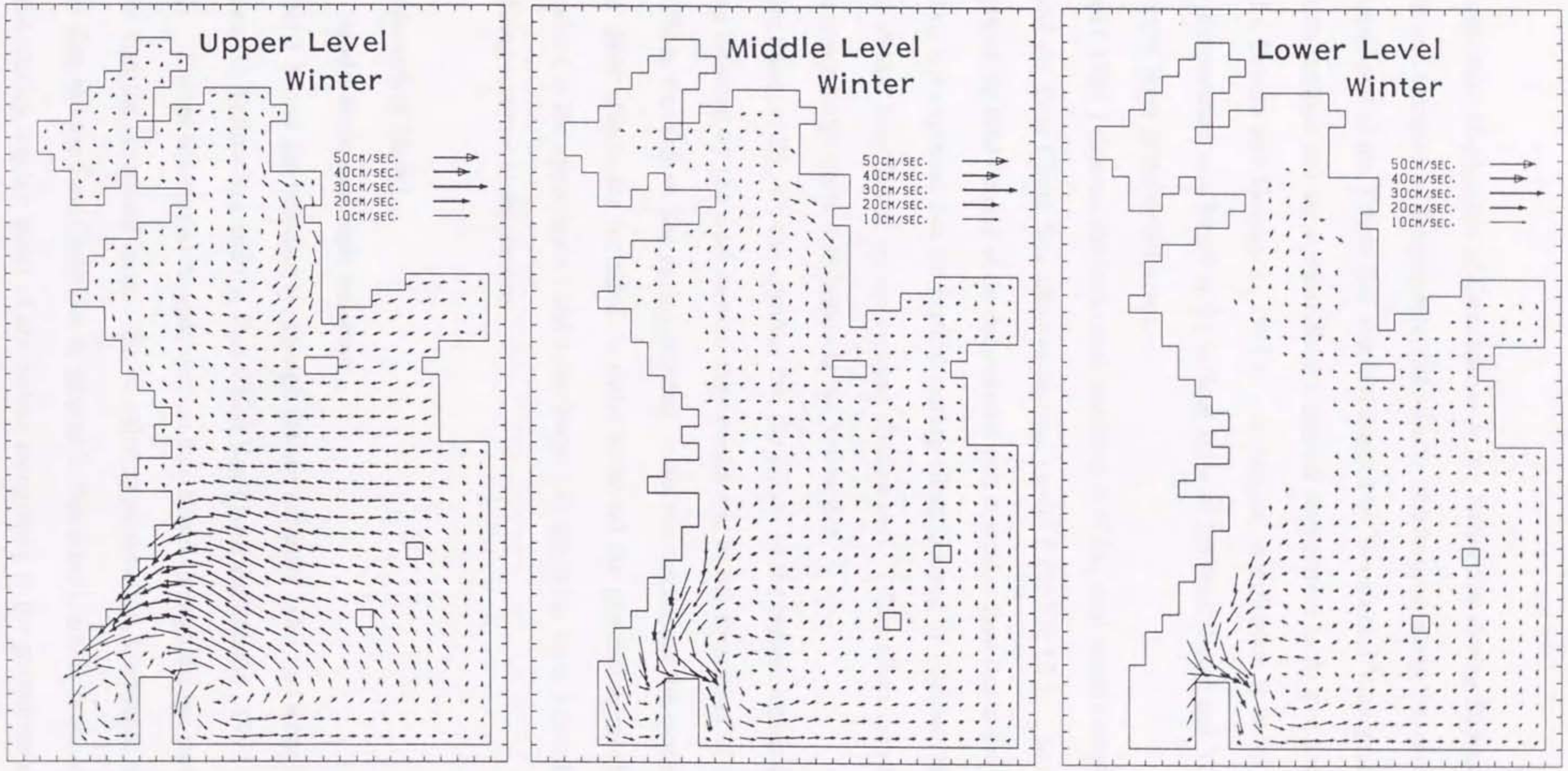

Fig.14 Water circulations in winter with wind stress and without density distribution.

3. Formation Mechanism of Circulations in the Yellow Sea during Summer

Seasonal variation of temperature and salinity distributions along the vertical cross section in the central part of the Yellow Sea was investigated by Tawara and Yamagata (1991). The observation stations and the vertical distributions of temperature in August and April are shown in Fig.15 (Tawara and Yamagata , 1991). In August, stratification is developed and the highest water temperature was found at the surface layer of the central part and YSBCW was found at the bottom layer in the deepest part.

Choi (1984) showed the horizontal distribution of M_2 tidal current amplitude in the Yellow Sea and the East China Sea using numerical model (see Fig.12). In the Yellow Sea, the strength of the tidal current at the deep central part is weaker than that at the surrounding shallow part, i.e., it is expected that the vertical mixing effect induced by tidal current at the deep central part is weaker than that at the surrounding shallow part. This effect may have some influence on the water temperature distribution in the Yellow Sea.

From these results, we can consider that the effects of the bottom topography and the vertical mixing induced by the tidal current may contribute to the formation of the circulations and YSBCW in the Yellow Sea during summer. So, we carried out the numerical experiments in which these effects are included, in order to reveal the generation mechanisms of an anti-clockwise (at the upper layer) and a clockwise (at the lower layer) circulations in the Yellow Sea during summer in this section.

3.1 Numerical Model

3.1.1 Model basin and basic equation

Table 1 shows the heat fluxes through the sea surface (Ishii and Kondo , 1987) and those between the Yellow Sea and the East China Sea (Ishii and Kondo , 1993) during the heating season. Except March and August, vertical heat fluxes through the sea surface are larger about 3 times than the horizontal ones. So, as a first approximation, horizontal heat flux between the Yellow Sea and the East China Sea is ignored in this model, and in order to reveal the effect of the tidal mixing and the effect of the bottom topography to the generation of an anti-clockwise

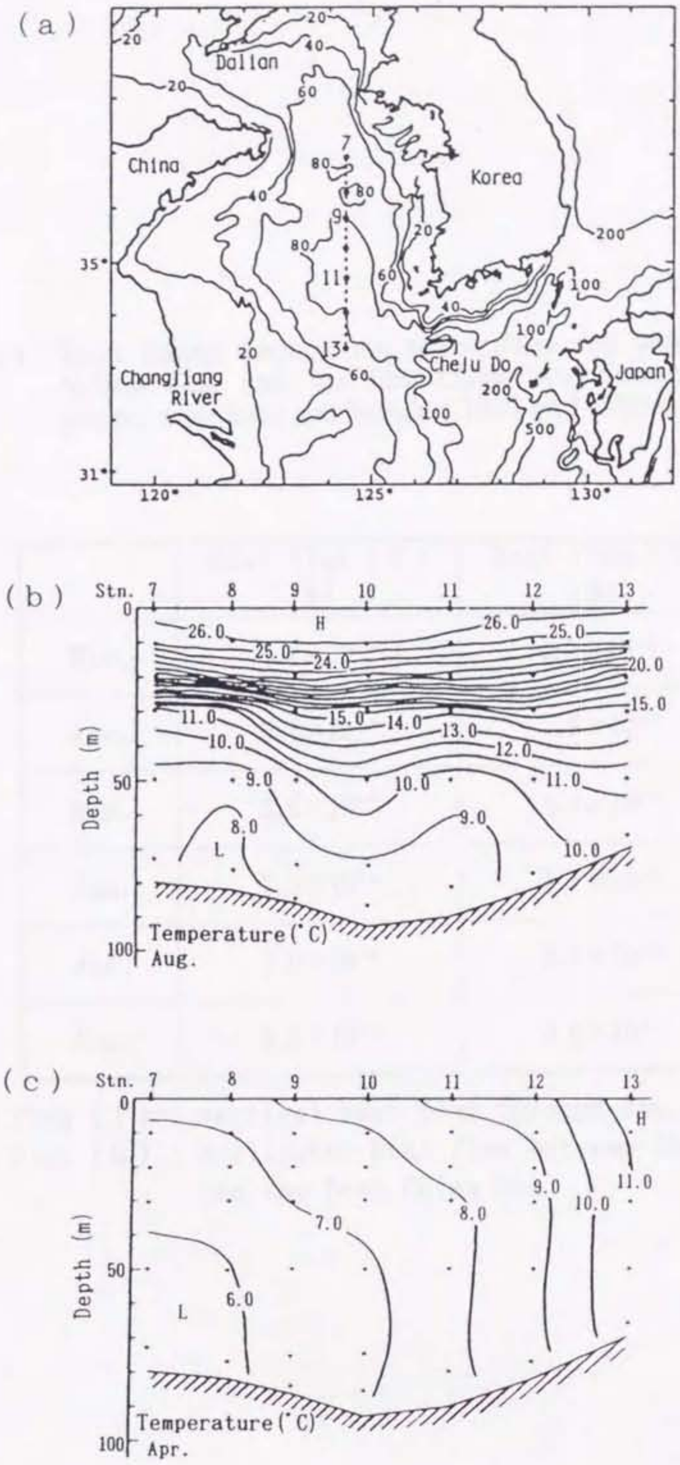

Fig.15 Map of the observation stations (a) and vertical distributions of temperature in August (b) and in April (c) obtained by averaging data during 1977 to 1986. After Tawara and Yamagata (1991).

Table 1 Heat fluxes through the sea surface and between the Yellow Sea and the East China Sea during heating period, after Ishii and Kondo (1987 and 1993).

	heat flux (I) (W)	heat flux (II) (W)
Mar.	1.2×10^{13}	-0.2×10^{13}
Apr.	5.7×10^{13}	1.5×10^{13}
May.	6.6×10^{13}	1.4×10^{13}
Jun.	7.3×10^{13}	1.1×10^{13}
Jul.	7.0×10^{13}	2.3×10^{13}
Aug.	5.2×10^{13}	3.6×10^{13}

heat flux (I) : vertical heat flux through the sea surface
heat flux (II) : horizontal heat flux between the Yellow Sea and the East China Sea

and a clockwise circulations in the Yellow Sea during summer, two kinds of the model basins which have a round shape are applied here. The bottom topography of the Yellow Sea (a) and the model regions (No.1 : (b) , No.2 : (c)) are shown in Fig.16. The No.1 model basin has a constant depth (80 m) and No.2 has a slope running along the coastal line in the model basin which represents the shelf slope in the Yellow Sea. This slope has a simple exponential form of $h = h_0 \exp(a x')$, where $h_0 = 20$ m, $a = 5.04 \times 10^{-6}$ (m^{-1}) and x' is offshore distance from the coast in meter. The maximum depth of the No.2 model basin is 80 m. The horizontal grid size is 25 km x 25 km and the water column is vertically divided into four levels (level 1 : 0–10 m, level 2 : 10–20 m, level 3 : 20–40 m, level 4 : 40 m – bottom).

Under the hydrostatic pressure, the Boussinesq and f–plain approximations, numerical model consist of the equations of motion, continuity and advection–diffusion of temperature. Using conventional notation, these equations on the Cartesian coordinate are as follows:

$$\frac{\partial u}{\partial t} + \left(u \frac{\partial u}{\partial x} + v \frac{\partial u}{\partial y} + w \frac{\partial u}{\partial z} \right) - fv$$
$$= - \frac{1}{\rho_0} \frac{\partial p}{\partial x} + \frac{\partial}{\partial x} \left(A_h \frac{\partial u}{\partial x} \right) + \frac{\partial}{\partial y} \left(A_h \frac{\partial u}{\partial y} \right) + \frac{\partial}{\partial z} \left(A_v \frac{\partial u}{\partial z} \right), \qquad (3\text{–}1)$$

$$\frac{\partial v}{\partial t} + \left(u \frac{\partial v}{\partial x} + v \frac{\partial v}{\partial y} + w \frac{\partial v}{\partial z} \right) + fu$$
$$= - \frac{1}{\rho_0} \frac{\partial p}{\partial x} + \frac{\partial}{\partial x} \left(A_h \frac{\partial v}{\partial x} \right) + \frac{\partial}{\partial y} \left(A_h \frac{\partial v}{\partial y} \right) + \frac{\partial}{\partial z} \left(A_v \frac{\partial v}{\partial z} \right), \qquad (3\text{–}2)$$

$$\frac{\partial p}{\partial z} = - \rho g , \qquad (3\text{–}3)$$

$$\frac{\partial u}{\partial x} + \frac{\partial v}{\partial y} + \frac{\partial w}{\partial z} = 0 , \qquad (3\text{–}4)$$

$$\frac{\partial T}{\partial t} + \left(u \frac{\partial T}{\partial x} + v \frac{\partial T}{\partial y} + w \frac{\partial T}{\partial z} \right) = K_h \left(\frac{\partial^2 T}{\partial x^2} + \frac{\partial^2 T}{\partial y^2} \right) + K_v \frac{\partial^2 T}{\partial z^2} \qquad (3\text{–}5)$$

where u, v, and w are the velocity components of x, y and z directions, respectively, f (8.34×10^{-5}

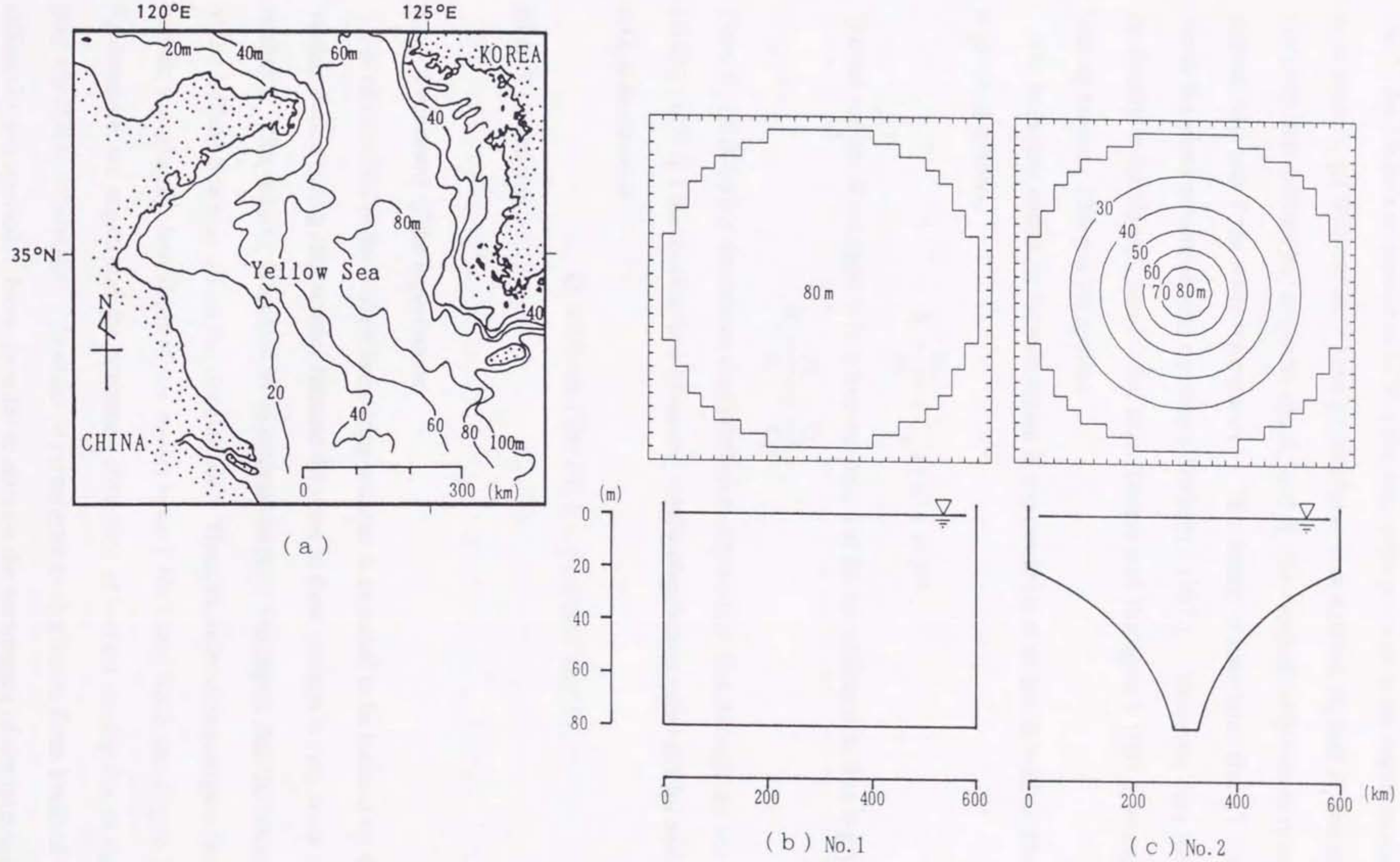

(a)

(b) No.1

(c) No.2

Fig.16 Bottom topography of the Yellow Sea (a) and two model basins (b)(c).

sec^{-1}) the Coriolis parameter at 35°N, t the time, p the pressure, ρ the water density, ρ_0 the reference density, g (980 cm sec^{-1}) the gravitational acceleration, A_h and K_h the horizontal eddy viscosity and diffusivity, respectively, A_v and K_v the vertical eddy viscosity and diffusivity, respectively, and T the water temperature. The density is calculated from T and salinity with use of the usual nonlinear state equation (Wadachi , 1987). However, only the effect of heat on density is considered, here. So, from Tawara and Yamagata (1991), averaged salinity in heating season (33.0 psu) is applied.

The boundary condition for momentum is slip condition at all lateral walls. The bottom stress is given as follows,

$$A_v \frac{\partial u}{\partial z} = C_b\, u\, (u^2 + v^2)^{1/2} . \qquad (3\text{-}6)$$

The sea surface is assumed to be a free-surface, and the sea surface heat flux is given as follows,

$$K_v \frac{\partial T}{\partial z} = \frac{Q_s}{C\rho} . \qquad (3\text{-}7)$$

Here, C_b (0.0026) is the bottom drag coefficient, Q_s the heat flux through the sea surface and C (0.932 cal/°C/g) the specific heat of water. Using observation value of Ishii and Kondo (1987), Q_s is assumed as,

$$Q_s = 350 \sin (2\pi t / T_y). \quad (\text{cal cm}^{-2} \text{ day}^{-1}) . \qquad (3\text{-}8)$$

Here, T_y is one year.

3.1.2 Procedure of the experiments

The circulations in the Yellow Sea during summer is expected to be induced by the sea surface heating during spring and summer because the wind in these seasons is very weak as discussed in section 2. So, only Q_s is applied as an external force. We expect that the bottom topography of the Yellow Sea may affect the circulations. Thus, in order to investigate the effect of the bottom topography, two kinds of the model basin (No.1 and No.2, see Fig.16) are applied. Furthermore, we expect that the horizontal difference of vertical mixing due to the tidal current may affect the circulations. In order to investigate such effects, three kinds of vertical eddy diffusivity are applied. Here, in order to restrain the occurrence of the internal waves at the interface between upper and lower levels of the model basin, the vertical eddy viscosity which is some larger than the vertical eddy diffusivity is applied. Three kinds of vertical eddy diffusivity, the corresponding vertical eddy viscosity and horizontal eddy diffusivity and viscosity are shown in the following.

1) The vertical eddy diffusivity are constant.

The vertical eddy viscosity and diffusivity are given as

$$A_v = 30 \quad (\mathrm{cm}^2\,\mathrm{sec}^{-1})\,, \tag{3-9}$$

$$K_v = 5 \quad (\mathrm{cm}^2\,\mathrm{sec}^{-1})\,, \tag{3-10}$$

and horizontal eddy viscosity and diffusivity are also constant as

$$A_h = K_h = 10^6 \quad (\mathrm{cm}^2\,\mathrm{sec}^{-1})\,. \tag{3-11}$$

2) The vertical eddy diffusivity varies with exponential form.

From the tidal current amplitude chart of Choi (1984), the vertical eddy viscosity and diffusivity are given as

$$A_v = 10\exp(3.66\mathrm{x}10^{-8}x^{*}) \quad \{ \text{maximum:}20 \} \quad (\mathrm{cm}^2\,\mathrm{sec}^{-1})\,, \tag{3-12}$$

$$K_v = \exp(7.68\mathrm{x}10^{-8}x^{*}) \quad \{ \text{maximum:}10 \} \quad (\mathrm{cm}^2\,\mathrm{sec}^{-1})\,, \tag{3-13}$$

and horizontal eddy viscosity and diffusivity are given as

$$A_h = K_h = 10^5\exp(7.68\mathrm{x}10^{-8}x^{*}) \quad \{ \text{maximum:}10^6 \} \quad (\mathrm{cm}^2\,\mathrm{sec}^{-1})\,, \tag{3-14}$$

where x^{*} is the distance from the center point of the model basin in cm.

3) The vertical eddy diffusivity depends on the Richardson number (James , 1977 ; Takeoka *et al.* , 1991).

The vertical eddy viscosity is given as

$$A_v = K_v + 10 \quad (\mathrm{cm}^2\,\mathrm{sec}^{-1})\,, \tag{3-15}$$

and according to Takeoka *et al.* (1991), the vertical eddy diffusivity are written as

$$K_v = \frac{K_0}{(1+\sigma Ri)^q} + K_b \tag{3-16}$$

where, $K_0 + K_b$ ($K_0 = 50.0$, $K_b = 0.1\ \mathrm{cm}^2\,\mathrm{sec}^{-1}$) is the diffusivity in the well-mixed state, σ (25.0) and q (0.7) the constants which are determined by Takeoka et al. (1991) and Ri the Richardson number. K_b is the background diffusivity which is added to prevent K_v becoming too small for large Ri. The Richardson number is given by

$$Ri = g\alpha \frac{\partial T/\partial z}{V} . \qquad (3\text{-}17)$$

Here, α (0.0002 °C^{-1}) is the thermal expansion coefficient and V the square of the vertical shear of the horizontal velocity. Under the approximation of the logarithmic law for the vertical distributions of the tidal current and wind–induced current, V is written as

$$V = \frac{1}{2} \{ \frac{u^*}{k(H-|z|)} \}^2 + (\frac{W^*}{kz})^2 + (\frac{\partial u}{\partial z})^2 . \qquad (3\text{-}18)$$

The first term on the right–hand side is the contribution of the shear of the tidal current, the second term that of the wind–induced current, the third term that of the density current, u^* and W^* the friction velocities of the tidal current and the wind–induced current, respectively, and k (0.41) the Karman constant. The friction velocities are given as

$$u^* = C_b^{1/2} u_a , \qquad (3\text{-}19)$$

$$W^* = (\rho_a/\rho)^{1/2} C_d^{1/2} W \qquad (3\text{-}20)$$

where ρ_a (0.0012 kg m^{-3}) is the air density, C_d (0.0013) the drag coefficient at the sea surface, W (2.0 m sec^{-1}) the wind speed, and u_a is the tidal current amplitude, that is given from Choi (1984) as

$$u_a = 120 - 20\exp\{ 0.447x10-8 (L/2 - x^*) \} \quad (cm\ sec^{-1}) . \qquad (3\text{-}21)$$

Here L (600 km) is the diameter of the model basin. In this case, horizontal eddy viscosity and diffusivity are given as Eq.(3–14).

3.1.3 Calculation results

The calculations of all cases are begun from the state of uniform water temperature (5°C), since that is the lowest water temperature in the Yellow Sea in April (Tawara and Yamagata , 1992. see Fig.15(c)). Cases of the numerical experiments are shown in Table 2. Figure 17 shows the temporal variations in kinetic energy of cases 1 and 2 which is defined as

$$KE = \sum_i (u_i^2 + v_i^2 + w_i^2) \qquad (3\text{-}22)$$

where u_i, v_i and w_i are u, v and w at a grid point i, respectively. The kinetic energies of both cases reach to the maximum on about 120 days. So, in this paper, the calculated results on 120

Table 2 Cases of the experiments.

Case	Depth	Kh,Ah	Kz,Az
1	No.1	exp	exp
2	No.2	const	const
3	No.2	exp	exp
4	No.2	exp	Ri

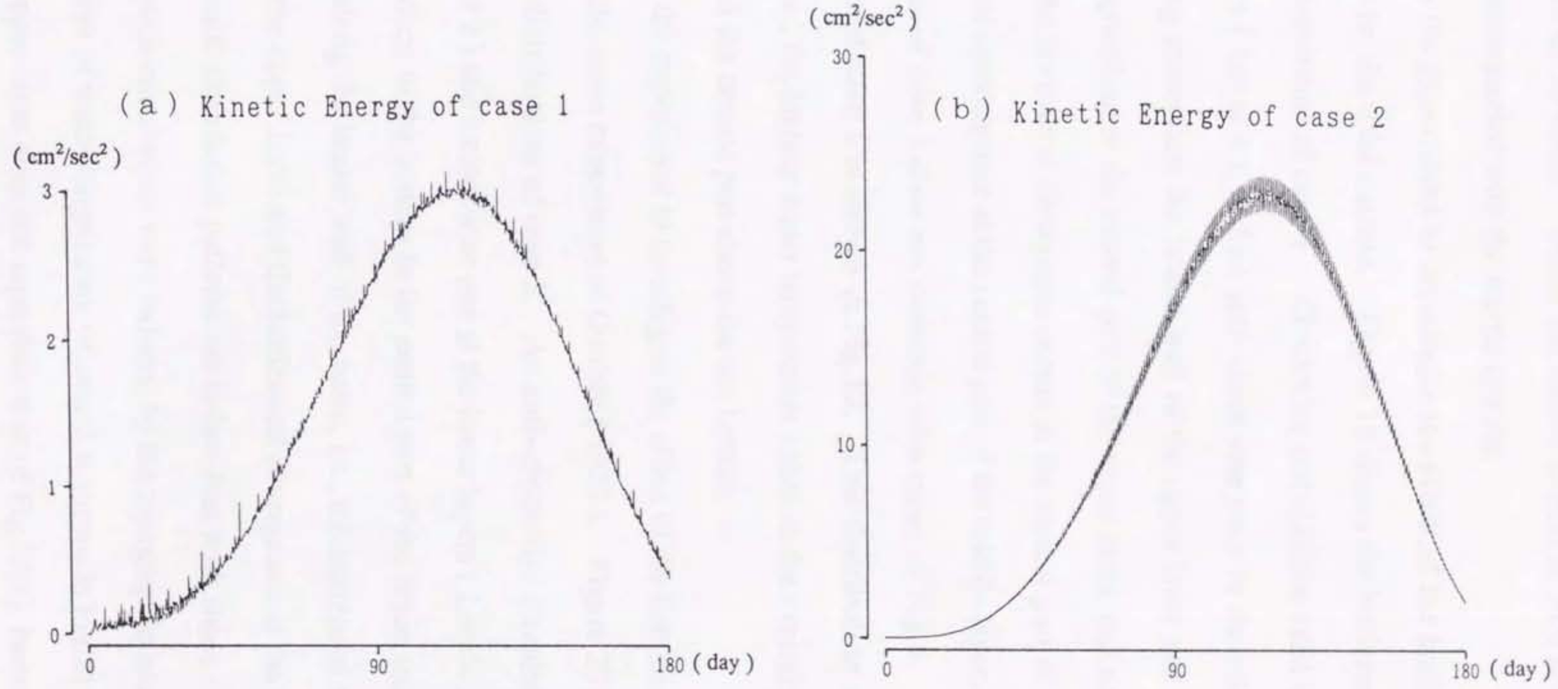

Fig.17 Time series of the kinetic energy in case 1 (a) and case 2 (b).

days are shown. Here, the smaller fluctuations of the kinetic energies of both cases have a period of about 20 hours. Since the inertia period is 20.9 hours at 35°N, these fluctuations should be accompanied with the inertia motion.

Case 1 is the experiment to investigate the effect of the horizontal variation in the vertical mixing due to the tidal current. Figure 18 shows the horizontal (left) and vertical (right) current distributions of case 1. Clockwise circulations exist in the upper (Level 1) and the lower layers (Level 4), and an anti-clockwise ones in the middle layers (Levels 2 and 3). Downwelling exists near the lateral wall of the upper layer and at the central part of the lower layer, and upwelling at the central part of the upper layer and near the lateral wall of the lower layer, i.e., the horizontal divergence occurs at the central part of the upper and lower layers and the horizontal convergence at the central part of the middle layer. However, horizontal circulation patterns of case 1 dose not coincide with those of Fig.6. Vertical distribution of water temperature of case 1 is shown in Fig.19. This distribution qualitatively reproduce that of Fig.15(b), i.e., the highest water temperature exists at the central part of the sub-surface and the lowest one at the central part above the sea bottom.

Case 2 is the experiment to investigate the effect of the bottom topography and this experiment is basically the same experiment as Oonishi (1975). Figure 20 shows the horizontal and vertical current distributions of case 2. An anti-clockwise circulation exists at the upper layers (Levels 1 and 2) and a clockwise one at the lower layers (Levels 3 and 4). Downwelling exists from the surface to the bottom in the central part of the basin and upwelling from the surface to the bottom along the lateral wall of the basin, i.e., the horizontal convergence occurs at the central part of the upper layer and the horizontal divergence at the central part of the lower layer. Such horizontal circulation patterns are coincident with those of Fig.6. Oonishi (1975) revealed that such circulations were induced by the topographic heat accumulation effect. Vertical distribution of water temperature of case 2 is shown in Fig.21. Water temperature distribution at the upper layer does not reproduce that of Fig.15(b), because the highest water temperature is seen at the sub-surface layer along the side wall. However, the water temperature distribution at the lower layer reproduces that of Fig.15(b), because the lowest water temperature

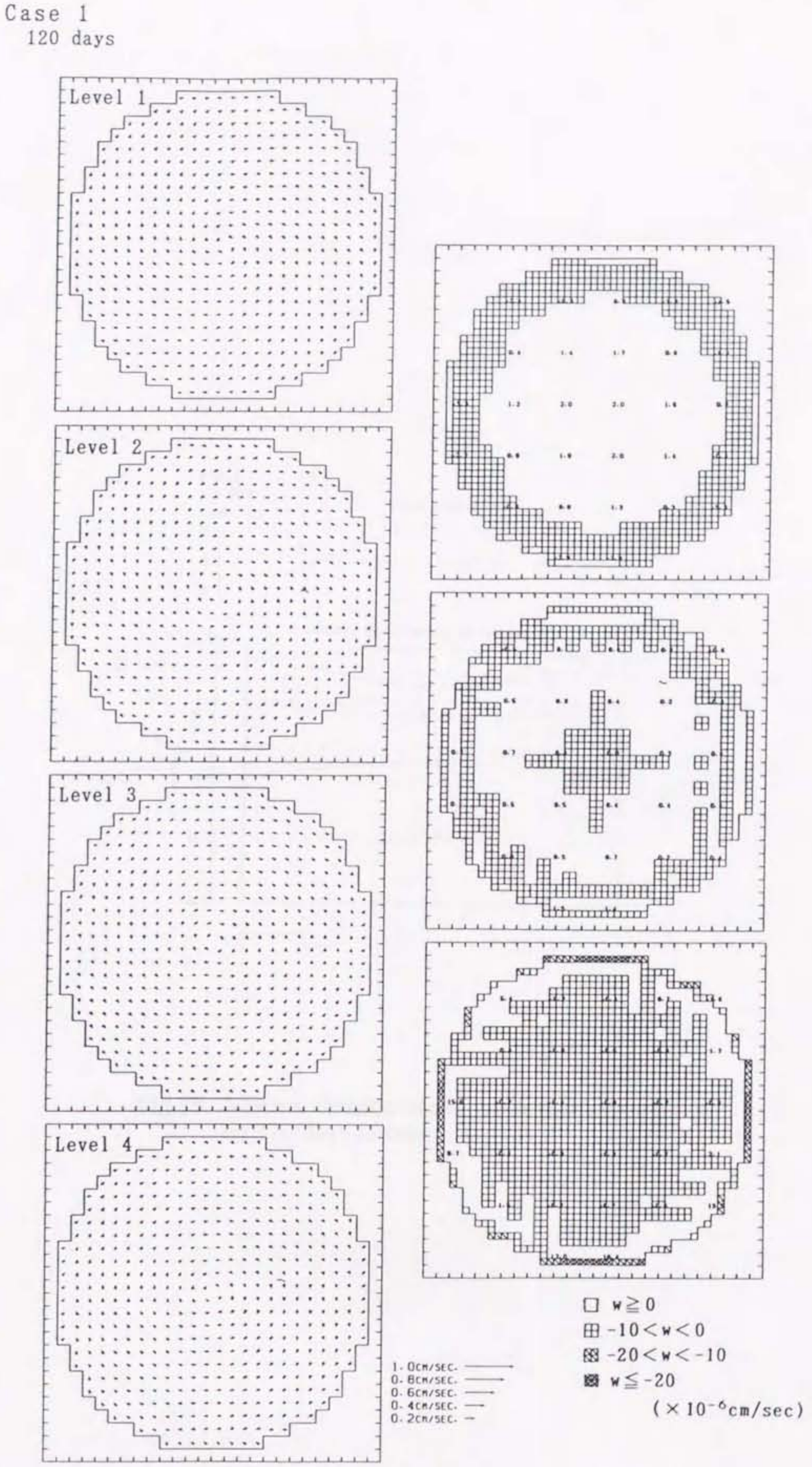

Fig.18 Horizontal current vectors (left) and vertical current distribution (right) on 120 days of case 1. Shadow areas show the downwelling.

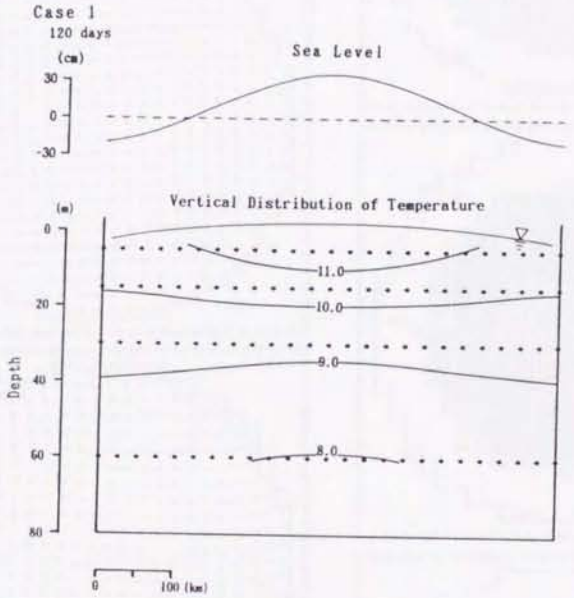

Fig.19 Vertical distribution of water temperature on 120 days of case 1.

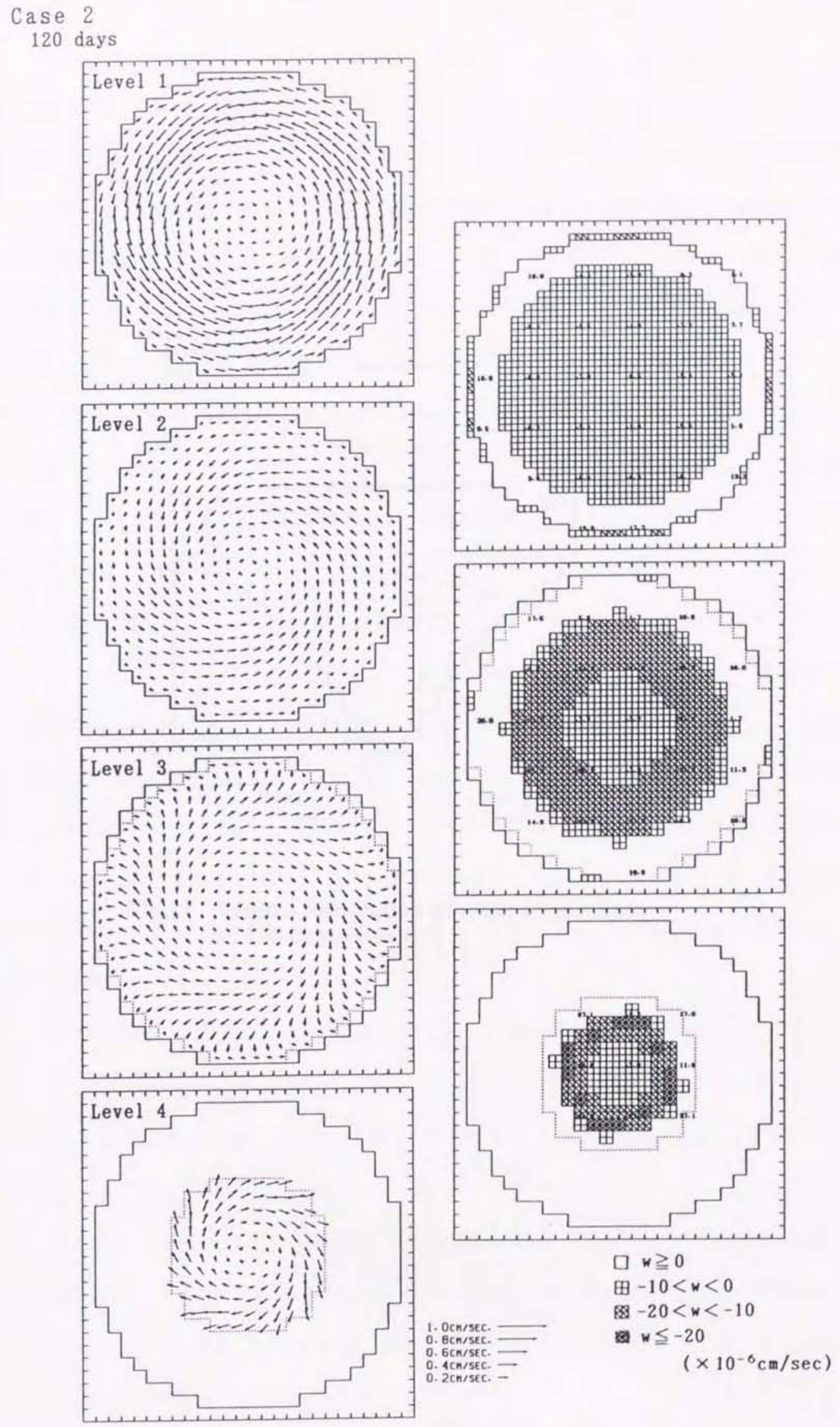

Fig.20 Horizontal current vectors (left) and vertical current distribution (right) on 120 days of case 2. Shadow areas show the downwelling.

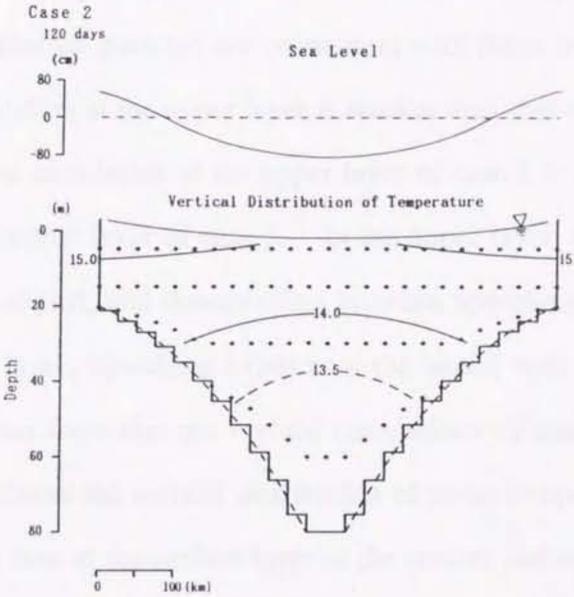

Fig.21 Vertical distribution of water temperature on 120 days of case 2.

exists just above the bottom of the deepest part.

From results of cases 1 and 2, we can expect that both effects (tidal mixing and bottom topography) contribute to the water temperature distribution and the generation of circulations in the Yellow Sea during summer. Thus, in case 3, an experiment which takes into account both effects is carried out. Figure 22 shows the horizontal and vertical current distributions of case 3. Horizontal circulation patterns are coincident with those of case 2, but the intensity of an anti–clockwise circulation at the upper layer is weaker than that of case 2. This is resulted from that a weak clockwise circulation at the upper layer of case 1 is superimposed on a strong anti–clockwise one at the upper layer of case 2. In the upper layer, upwellings exist near the lateral wall and at the central part, and downwelling between upwellings with doughnut–like distribution. In the lower layer, upwelling exists near the lateral wall and downwelling at the central part. This is resulted from that the vertical circulations of case 1 is superimposed on once of case 2. Figure 23 shows the vertical distribution of water temperature of case 3. The highest water temperature is seen at the surface layer of the central part and the lowest one just above the bottom of the deepest part. Such distribution pattern reproduces that of Fig.15(b), although the developed thermocline is not reproduced. Various kinds of the vertical eddy diffusivity and viscosity which have exponential forms are applied. However, the thermocline is not developed in these experiments.

In case 4, the vertical eddy viscosity which depends on the Richardson number (Eq.(3–16)) is applied, i.e., an experiment of case 4 is carried out in order to reproduce the developed thermocline. Horizontal circulation patterns of case 4 are coincident with that of case 2, although the intensity of a surface anti–clockwise circulation is weak. The vertical water temperature distribution of case 4 is shown in Fig.24. The thermocline develops at the sub–surface layer and the low temperature water mass is formed at the bottom of the deepest part of the basin with dome–like shape. Such water temperature distribution well reproduces that of Fig.15(b).

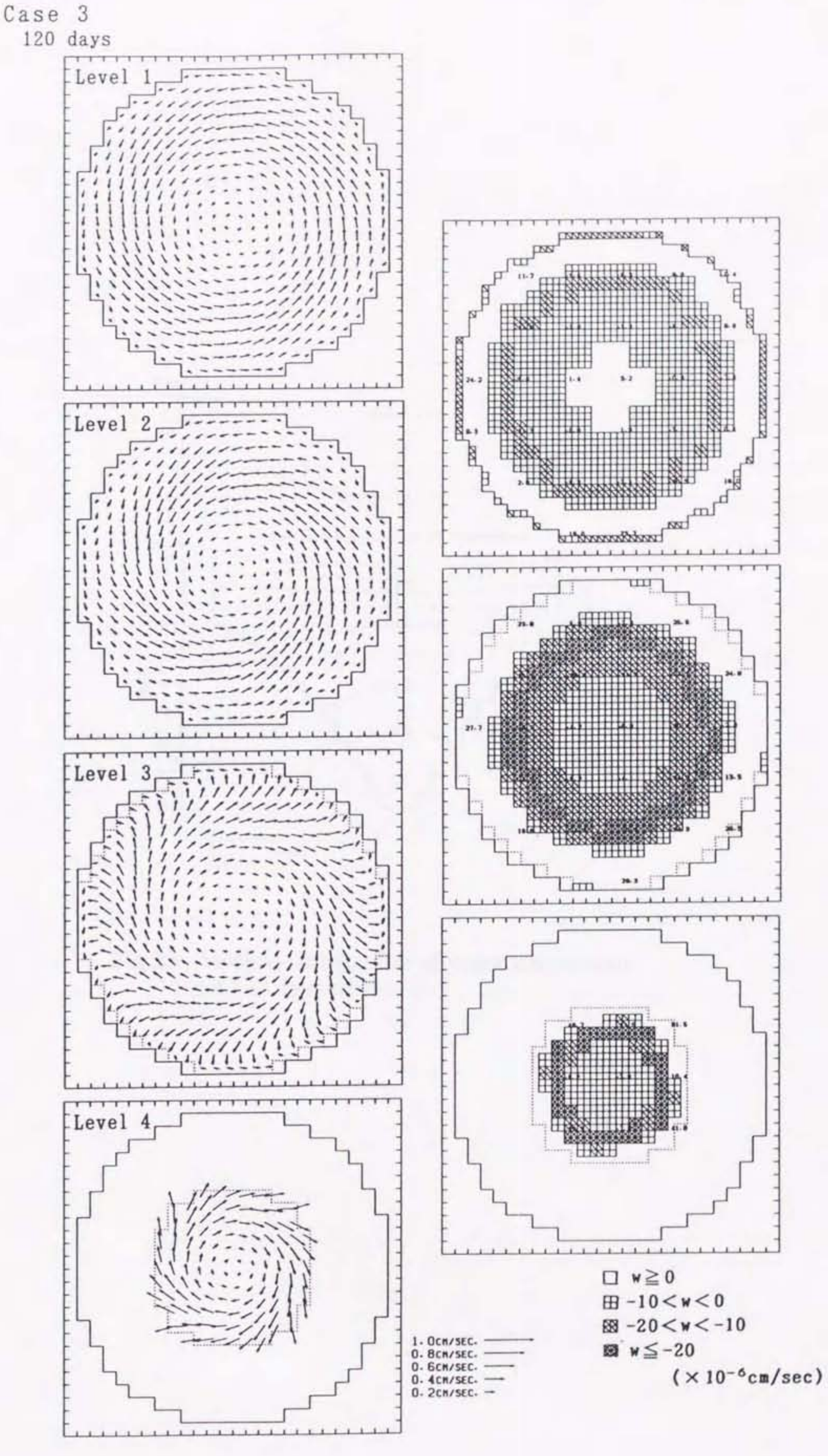

Fig.22 Horizontal current vectors (left) and vertical current distribution (right) on 120 days of case 3. Shadow areas show the downwelling.

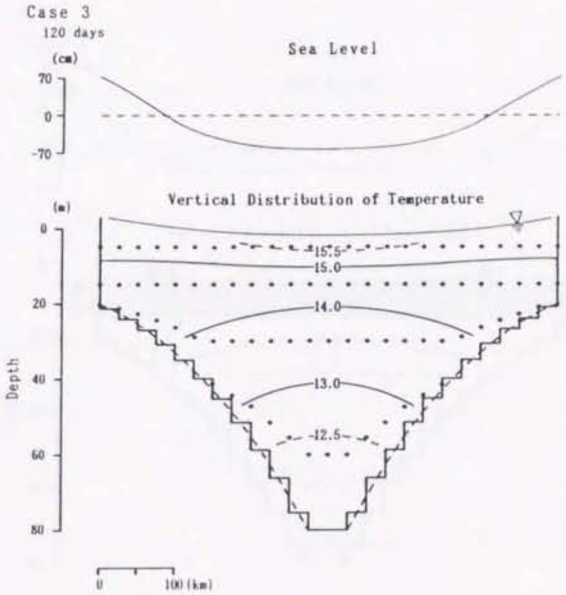

Fig.23 Vertical distribution of water temperature on 120 days of case 3.

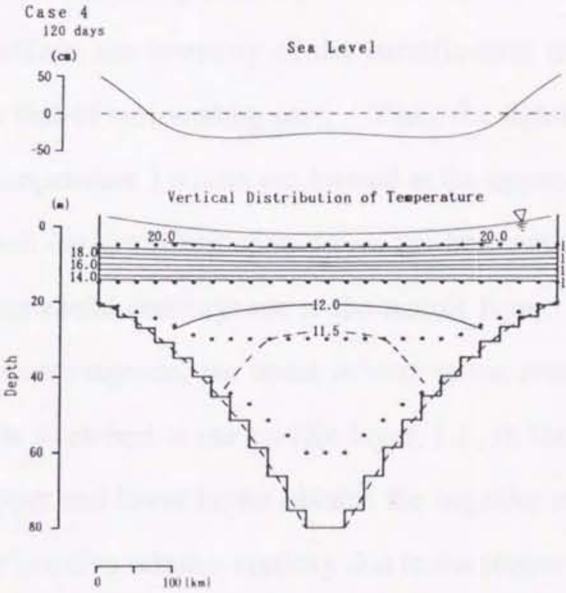

Fig.24 Vertical distribution of water temperature on 120 days of case 4.

3.2 Discussions

The circulations in the Yellow Sea during summer are mainly induced by the sea surface heating and are affected by the vertical mixing of the tidal current and the bottom topography. The schematic generation mechanisms of the circulations of cases 1 and 2 are shown in Fig.25. In case 1, the homogeneous water which is formed by the sea surface cooling in winter begins to stratify due to the sea surface heating in spring. However, due to the horizontal difference of the tidal vertical mixing effect, the intensity of the stratification in the central part of the basin becomes stronger than that of surrounding part. Thus, the lightest (highest temperature) and the heaviest (lowest temperature) waters are formed at the upper and lower layers in the central part of the basin. Such density distribution drives the horizontal divergences at the upper and lower layers and the horizontal convergence at the middle layer. Accompanied by such horizontal divergences and convergence, the water column in the central part is shrunk at the upper and lower layers and is stretched at the middle layer, i.e., in the central part of the basin, the water column at the upper and lower layers obtains the negative relative vorticity and that at the middle layer obtain the positive relative vorticity due to the conservation law of potential vorticity in the rotational fluid. Consequently, the clockwise circulations are developed at the upper and lower layers and an anti-clockwise one at middle layer. Here, the largest vertical velocity of the case 1 has an order of 10^{-5} cm $\sec^{-1}$. So, the vertical maximum movement of the water particles are only several meters per 180 days, i.e., the water particles obtain the positive (negative) relative vorticity at every time during heating season. Hence, the horizontal circulations of case 1 are maintained during heating season with the structure of the quasi geostrophic current and the sea level of the central region rises due to the geostrophic adjustment.

In case 2, the initial condition is the same as that of case 1. At the beginning of the surface heating, the lighter (higher temperature) water is distributed on the shallow area and the heavier (lower temperature) water in the central deeper part due to the topographic heat accumulation effect. Such density distribution drives the horizontal convergence in the upper layer and the horizontal divergence in the lower layer. Accompanied by such horizontal convergence and

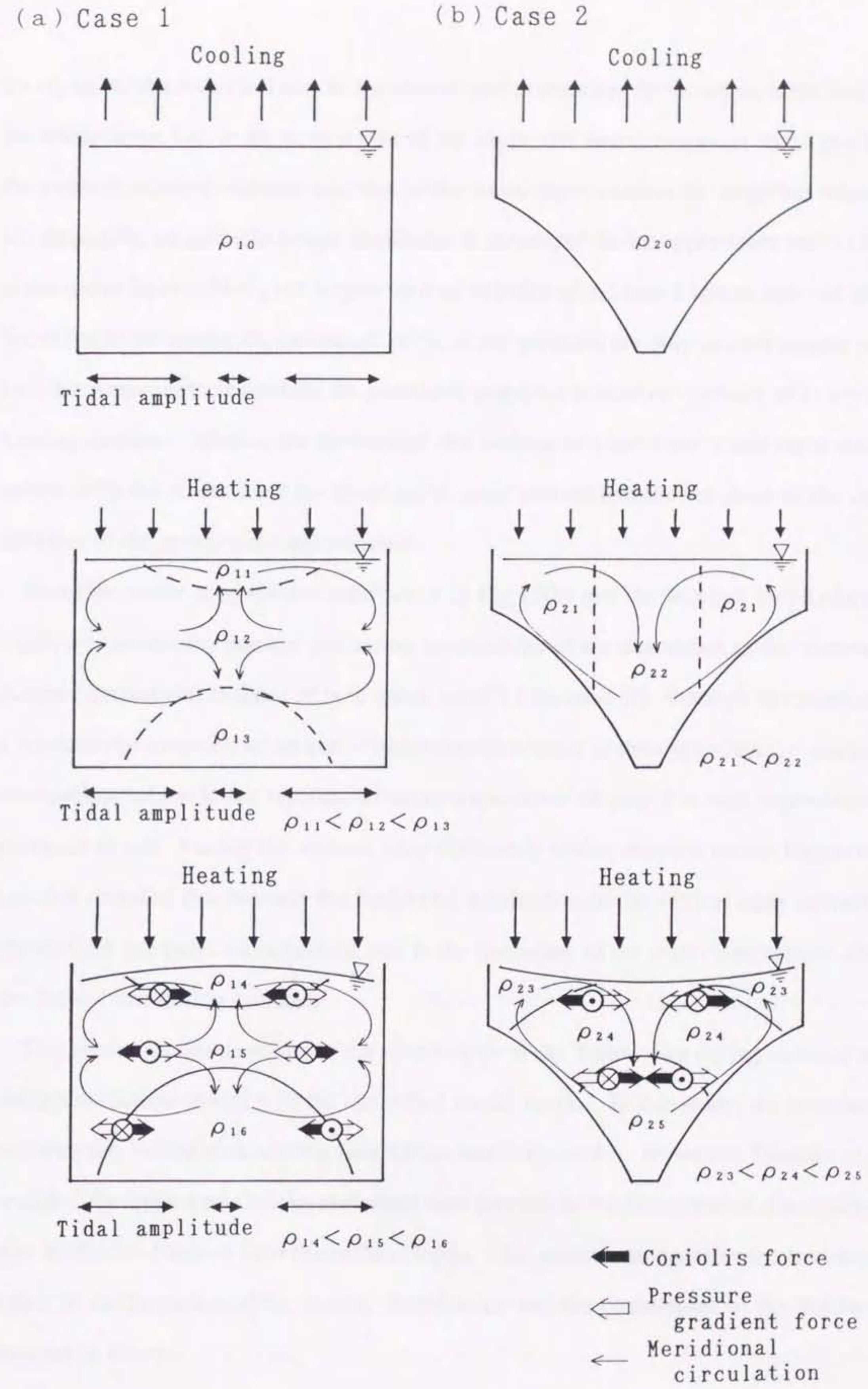

Fig.25 Schematic figure of the generation mechanisms of the circulations in case 1 (a) and case 2 (b).

divergences, the water column in the central part is stretched in the upper layer and is shrunk in the lower layer, i.e., in the central part of the basin, the water column at the upper layer obtains the positive relative vorticity and that at the lower layer obtains the negative relative vorticity. Consequently, an anti-clockwise circulation is developed at the upper layer and a clockwise one at the lower layer. Here, the largest vertical velocity of the case 2 has an order of 10^{-5} cm sec^{-1}. So, the vertical maximum movement of the water particles are only several meters per 180 days, i.e., the water particles obtain the positive (negative) relative vorticity at every time during heating season. Hence, the horizontal circulations of case 2 are maintained during heating season with the structure of the quasi geostrophic current and the sea level of the central region falls due to the geostrophic adjustment.

From the water temperature distribution in Fig.15(b) and the summer circulations pattern in Fig.6, it is concluded that the generation mechanisms of the circulation in the Yellow Sea during summer correspond to those of both cases 1 and 2 (i.e. case 3), although the mechanism of case 1 weaken the intensity of an anti-clockwise circulation at the upper layer. Furthermore, the thermocline which is not reproduced in the experiment of case 3 is well reproduced in the experiment of case 4 using the vertical eddy diffusivity which depends on the Richardson number, i.e., it is revealed that not only the horizontal distribution of the vertical eddy diffusivity but also the vertical one plays an important role in the formation of the water temperature distribution in the Yellow Sea during summer.

The generation mechanisms of the circulations in the Yellow Sea during summer are revealed using a numerical model with the simplified model basin. In this study, the horizontal heat flux between the Yellow Sea and the East China Sea is ignored. However, Takeoka *et al.* (1991) revealed the importance of the horizontal heat process in the formation of the density stratification in Hiuchi-Nada of Seto Inland Sea, Japan. So, we have to consider the horizontal heat flux effect to the formation of the density stratification and the circulations of the Yellow Sea during summer in future.

4. *Formation and Variation Mechanism of a Clockwise-Circulation during Winter in the Yellow Sea*

In winter, a steady clockwise circulation is developed from surface to bottom in the Yellow Sea, while an anti-clockwise one in the northern part of the East China Sea as discussed in section 2. On the other hand, a clockwise circulation was not so developed under the wind forced condition in the sequential pattern of the current vector of Hsueh et al. (1986).

From current observation results at several points of the Yellow Sea in winter, Hsueh and Pang (1989) indicated that the fluctuating part of the current field with several days period dominated rather than the steady circulations and it was related with the monsoon wind variations. Furthermore, they revealed that these currents are accompanied by the shelf waves which are generated by the northerly periodical wind forcing.

These results suggest two facts : the steady part and the fluctuating part of the current field exist simultaneously in the Yellow Sea during winter, and both current fields are generated by the winter wind forcing. However, the formation and variation mechanisms of such clockwise circulation in the Yellow Sea and dynamical relationship between the clockwise circulation (steady part) and the fluctuating part of the current field are still unknown.

In this section, we aim to reveal the formation and variation mechanisms of a clockwise circulation in the Yellow Sea during winter, and the importance of shelf waves to the formation mechanisms of water circulations is investigated using the wind forced numerical model.

4.1 Model Description

The oceanic condition of the Yellow Sea in winter was investigated by Tawara and Yamagata (1991) using observed hydrographic data obtained form 1964 to 1987. The averaged vertical distribution of temperature and salinity in February is shown in Fig.26. Temperature and salinity distributions are approximately uniform in the vertical direction and the horizontal density difference between the Stn.7 ($\sigma_t \fallingdotseq 25.80$) and Stn.13 ($\sigma_t \fallingdotseq 25.83$) is a little. Namely, this area could be regarded as approximately homogeneous waters. The sea surface winds were computed over the adjacent seas of Korea from the twice-daily weather maps from year 1978 to 1987 (Na et.al.

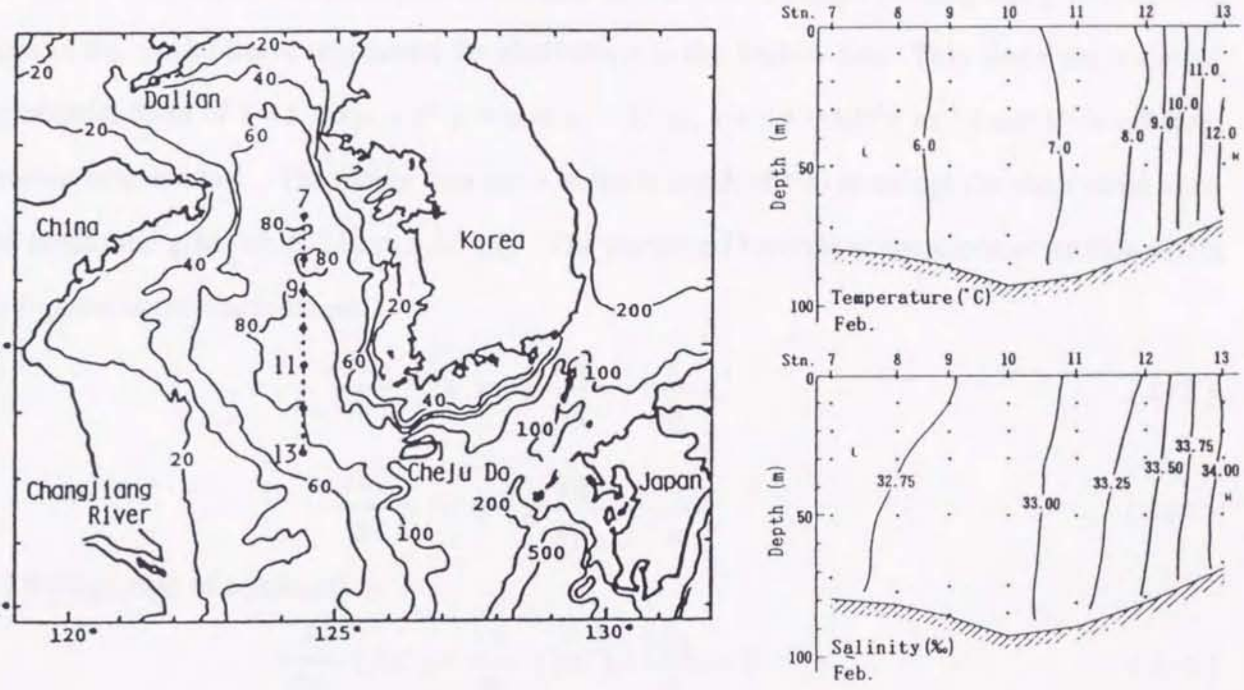

Fig.26 Map of the observation stations and vertical distribution of temperature and salinity at February obtained by averaging data during 1977 to 1986.
After Tawara and Yamagata (1991)

, 1992). Figure 27 shows the distribution of monthly mean wind stress in February. The north–westerly wind dominates at the Yellow Sea. Therefore, we attempt the north–westerly wind forced barotropic model with the simplified basin in order to understand the detailed dynamics of the formation and variation mechanisms of water circulations during winter in the Yellow Sea. Figure 28 shows the map of the Yellow Sea and the East China Sea region (a) and the model region (b) with the wind direction and X–Y coordinate. The model basin represents the Yellow Sea and the northern part of the East China Sea. A slope running along the northern coast in the model basin represents the shelf slope in the Yellow Sea. This slope has a simple exponential form of $h = h_0 \exp(a x^*)$, where $h_0 = 15$ m, $a = 8.43 \times 10^{-6}$ (m^{-1}) and x^* is offshore distance from a coast. The model area has a uniform depth of 100 m except the shelf slope area. The horizontal grid size is 25 km x 25 km. The linearized barotropic equations of motion under the f–plane approximation are

$$\frac{\partial U}{\partial t} - fV = - g \frac{\partial \eta}{\partial x} + \frac{\tau_x}{h}, \qquad (4\text{–}1)$$

$$\frac{\partial V}{\partial t} + fU = - g \frac{\partial \eta}{\partial y} + \frac{\tau_y}{h} \qquad (4\text{–}2)$$

and the equation of continuity is

$$\frac{\partial}{\partial x}(hU) + \frac{\partial}{\partial y}(hV) + \frac{\partial \eta}{\partial t} = 0 \qquad (4\text{–}3)$$

where U and V are the depth–averaged components of velocity in x and y directions, respectively; η is the elevation of sea surface from its mean level; τ_x and τ_y are the x and y components of wind stress; g is the acceleration due to gravity; h is the water depth and f (8.34×10^{-5} sec^{-1}) is the Coriolis parameter.

The boundary condition for momentum is slip condition at all lateral walls. The wind stress at the sea surface is given by

$$\tau_x = \rho_a C_d W_x (W_x^2 + W_y^2)^{1/2}, \qquad (4\text{–}4)$$

$$\tau_y = \rho_a C_d W_y (W_x^2 + W_y^2)^{1/2} \qquad (4\text{–}5)$$

where ρ_a (0.0012 g cm^{-3}) is the air density; C_d (0.0013) is the sea surface drag coefficient; W_x and W_y are the x and y components of the wind vector, respectively.

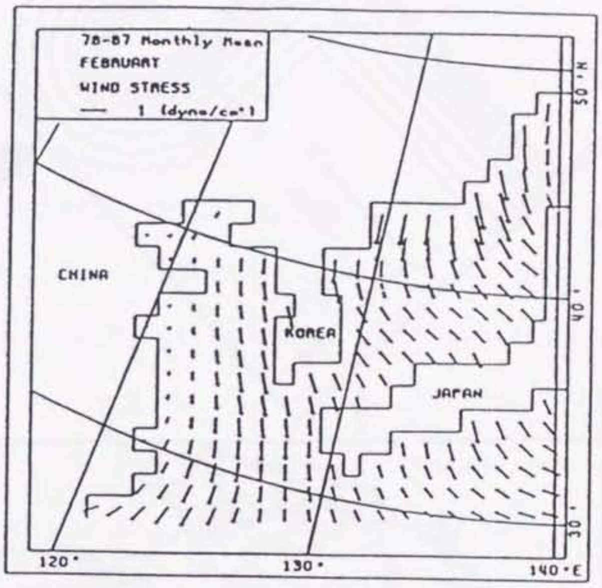

Fig.27 Distribution of monthly mean wind at February computing from the twice-daily weather maps for the period 1978 to 1987. After Na et al. (1992)

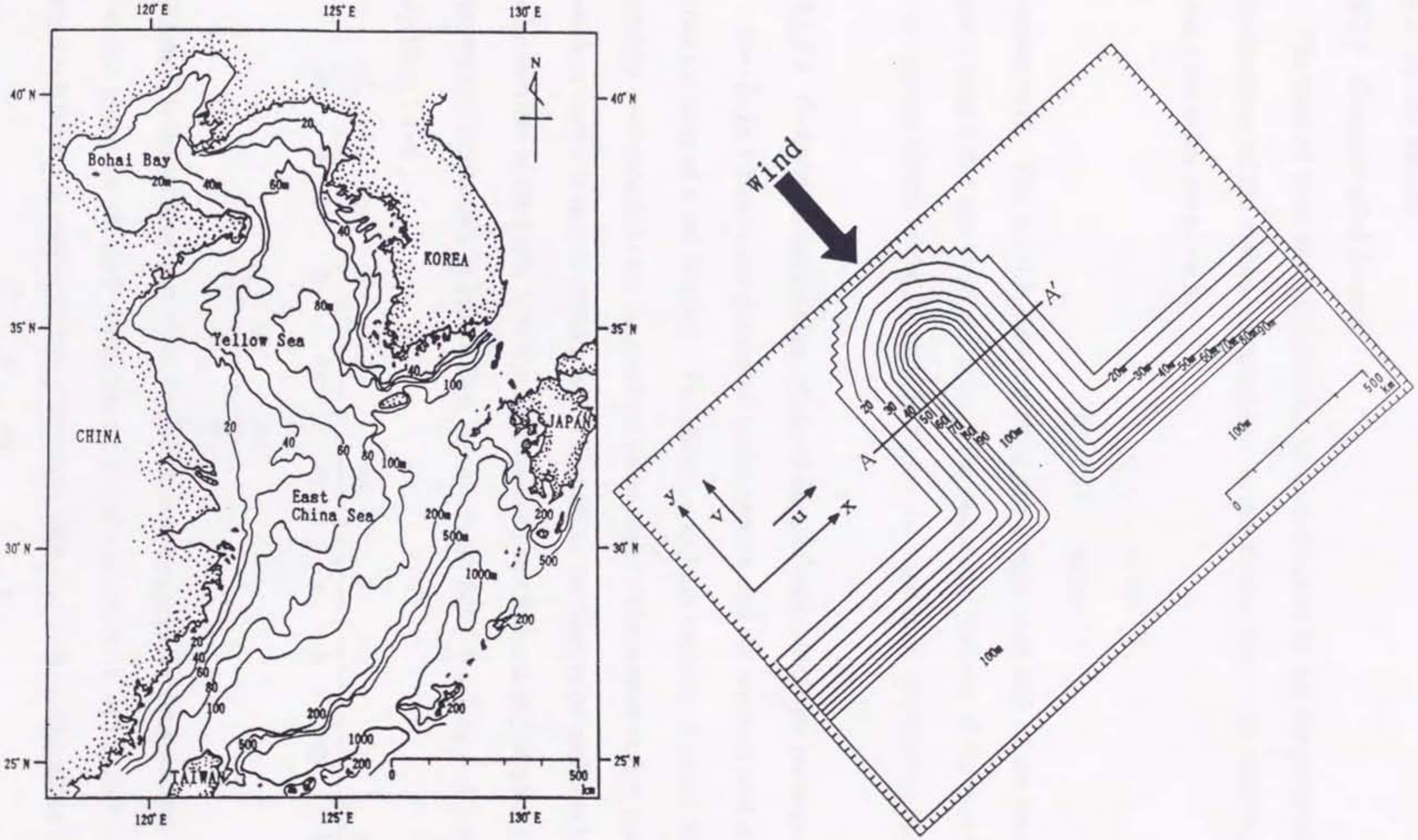

(a)

(b)

Fig.28 Map and bottom topography of the Yellow Sea and the East China Sea (a) and model area (b) with the wind direction and x−y coordinate.
Numbers show the depth in meter.

4.2 Model Results

4.2.1 Constant wind forcing

The case of constant wind forcing is carried out to reveal the generation and maintenance mechanisms of the clockwise circulation in the Yellow Sea. The wind vector components of x and y direction are given by

$$W_x = 0 \quad (\mathrm{m\ sec^{-1}}), \qquad (4\text{-}6)$$

$$W_y = -5 \quad (\mathrm{m\ sec^{-1}}) \qquad (4\text{-}7)$$

respectively. This wind is blowing along the longitudinal axis of the basin. The wind forcing starts from 0 day and stops at 5 days. The sequential patterns of the current vector during wind blowing are shown in Fig.29, and those after the wind stops are shown in Fig.30.

4.2.1.1 Generation mechanism of clockwise and anti-clockwise vortices in the basin

Two large vortices are generated in the eastern and the western part of the basin at 0.5 day after the start of wind forcing. The diameter of both vortices is about 600 km which approximately corresponds to the longitudinal basin scale. The eastern vortex is a clockwise, while the western vortex is an anti-clockwise. Generation mechanism of such clockwise and anti-clockwise vortices in the basin was already explained by Ohshima and Miyake (1990) as an example for winter circulations in Funka Bay, Japan. From Eqs.(4-1) - (4-3), we obtain the vorticity equation (4-8).

$$\frac{\partial \zeta}{\partial t} - \frac{f}{h}\frac{\partial \eta}{\partial t} - \frac{f}{h}\left(U\frac{\partial h}{\partial x} + V\frac{\partial h}{\partial y} \right) - \frac{\partial}{\partial x}\left(\frac{\tau_y}{h} \right) + \frac{\partial}{\partial y}\left(\frac{\tau_x}{h} \right) = 0, \qquad (4\text{-}8)$$

$$\zeta = \frac{\partial V}{\partial x} - \frac{\partial U}{\partial y}.$$

Where ζ is the relative vorticity. Under the nondivergence approximation, we consider the local balance along the channel which has a vertical section A-A' of Fig.28(b) and spatially uniform wind is blowing in only negative-y direction, then Eq.(4-8) is simplified to

$$\frac{\partial \zeta}{\partial t} = \frac{f}{h} U \frac{\partial h}{\partial x} + \frac{\partial}{\partial x}\left(\frac{\tau_y}{h} \right). \qquad (4\text{-}9)$$

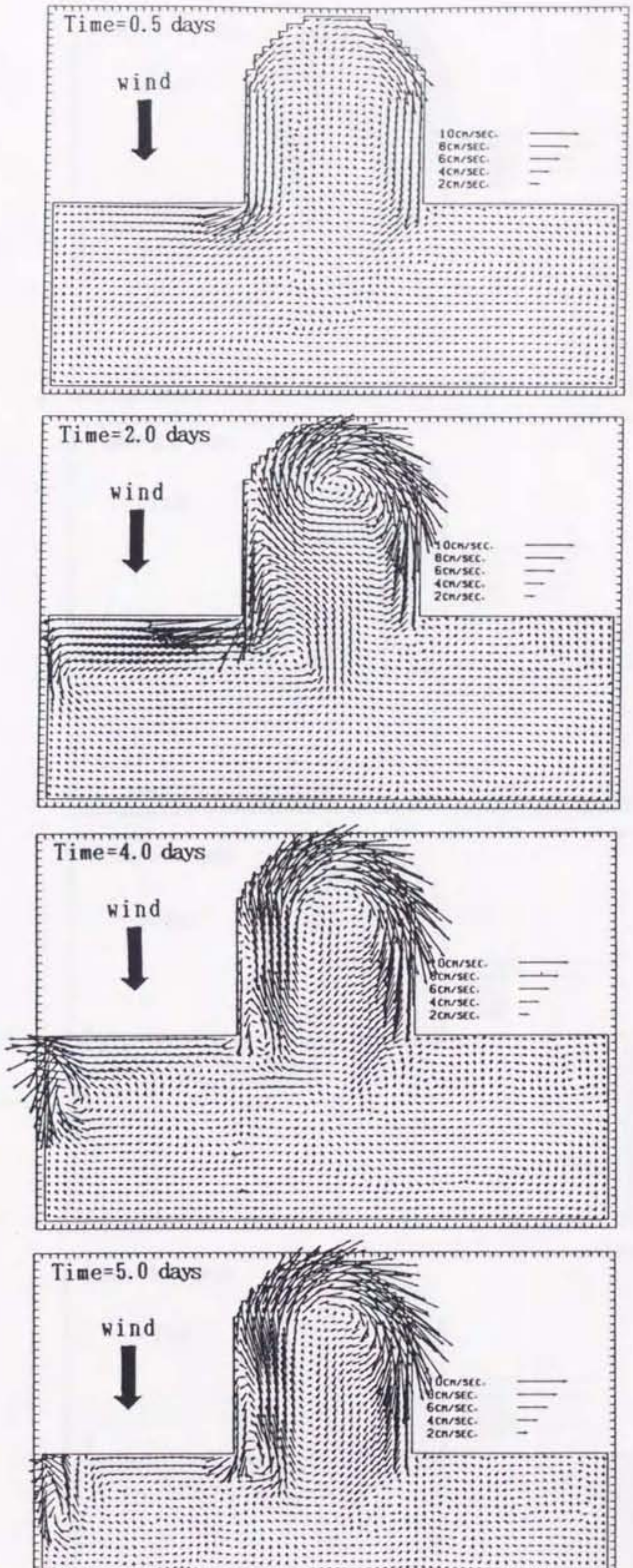

Fig.29 Time series of the current vectors. The north-westerly (negative-y direction) wind, which has constant velocity (5m/sec.), is blowing.

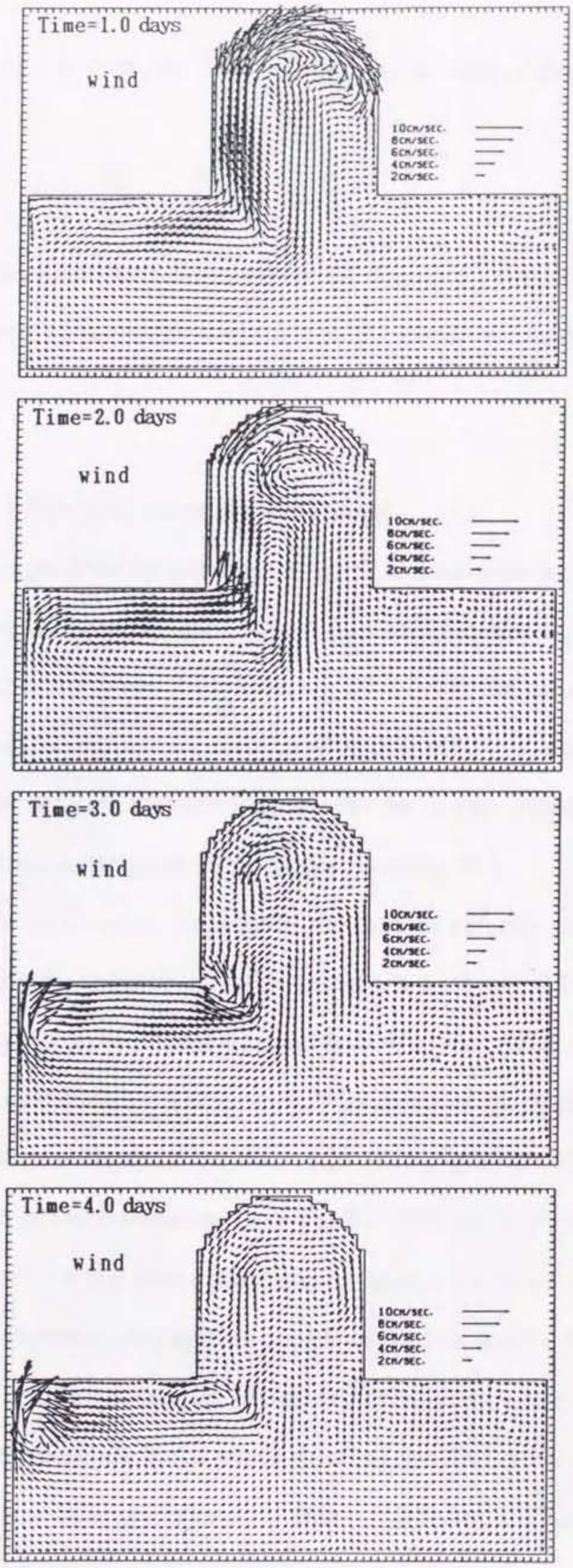

Fig.30 Time series of the current vector after the wind stops.

The initial condition of u is 0 cm sec^{-1}. Therefore, at the start of the calculation, we obtain Eq.(4–10).

$$\frac{\partial \zeta}{\partial t} = \frac{\partial}{\partial x}\left(\frac{\tau_y}{h}\right). \qquad (4\text{–}10)$$

Equation (4–10) means that the relative positive (negative) vorticity is provided at the south-western (north-eastern) part of the basin due to the north-westerly wind forcing on the shelf slope.

4.2.1.2 Propagation of vortices along the shelf slope

Both vortices propagate looking the coast to its right hand side as time goes on. The eastern vortex becomes strong and stays at the northern part of the basin in 4 days. This vortex stably exists during wind blowing (see 5 days of Fig.29). On the other hand, the western anti-clockwise vortex is pressed against the west coast and its offshore scale reduces. In about 3 days after the wind stops, it is found that the large clockwise vortex propagates away southward and relatively, a few small vortices appear in the basin (see Fig.30).

Figure 31 shows the time–space diagram of the current velocity component along the coast. The direction of looking the coast to the left hand side is positive. Most remarkable propagation speed is approximately 4.2 m sec^{-1} and the propagation speeds (about 21.5 m sec^{-1}, 1.2 m sec^{-1} and 0.5 m sec^{-1}) are also found. The propagation speed of the Kelvin wave is approximately 21.5 m sec^{-1} ($\sqrt{g\bar{h}}$: $\bar{h}$ is mean depth of the section B–B' of Fig.32). The Kelvin wave propagates away at the early stage of the calculation from Fig.31. Figure 32 shows the dispersion relationship at the section B–B' for the lower three modes of shelf waves (solid lines). Dotted lines show the observed or expected propagation speeds of 21.5 m sec^{-1} (Kelvin wave), 4.2 m sec^{-1}, 1.2 m sec^{-1} and 0.5 m sec^{-1} respectively. From this relationship, it is found that the propagation speed of 4.2 m sec^{-1} corresponds to the phase speed of the first mode non-dispersive shelf wave which has a wave-length of approximately 1,100 – 1,200 km. This wave-length agrees with twice of the basin scale.

Both vortices propagate looking the coast to the right hand side as the first mode shelf waves.

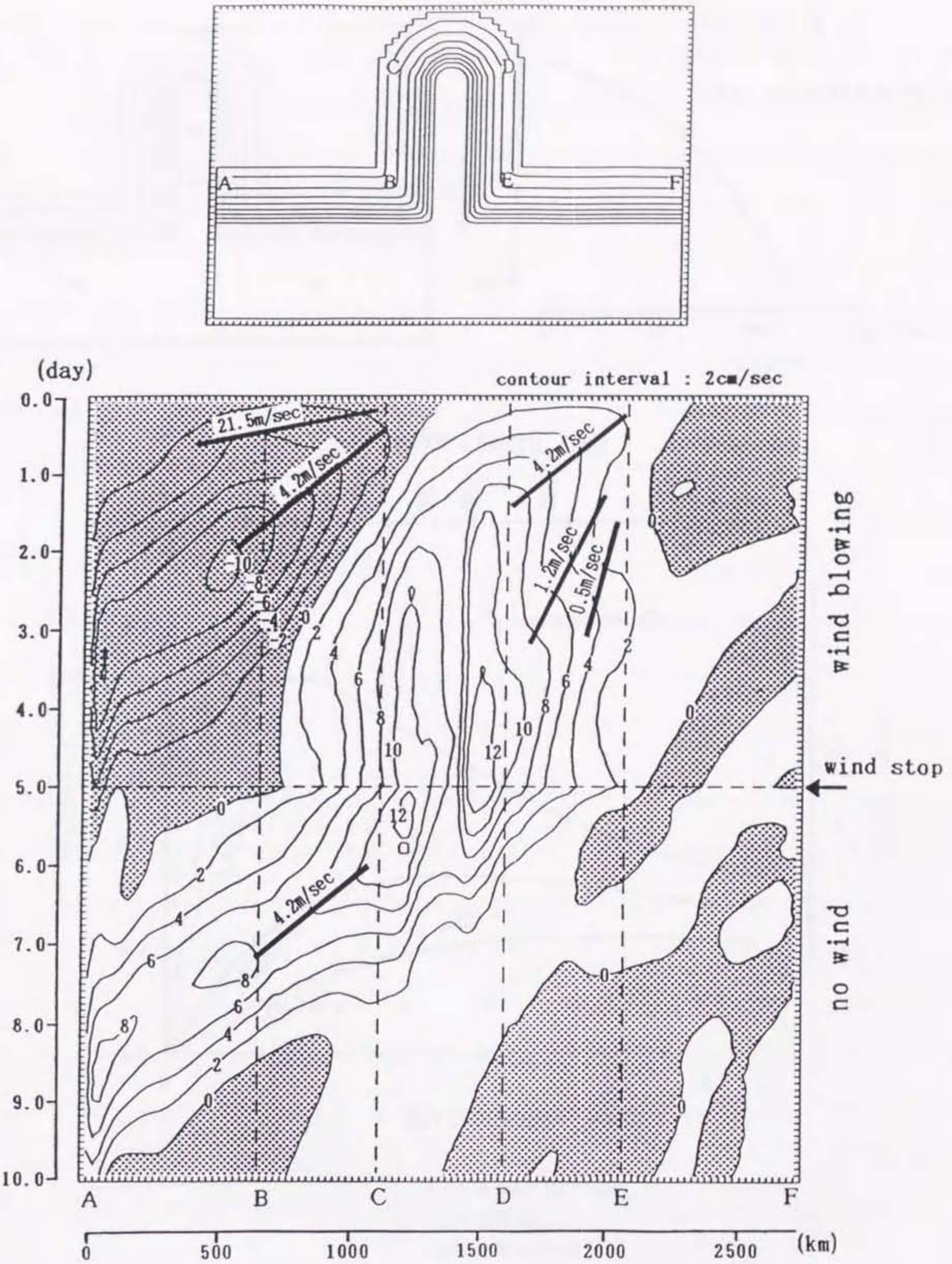

Fig.31 Time–space diagram of the current velocity component along the line ABCDEF of upper panel. The direction of looking the coast to the left hand side is positive. Negative velocity zones are dotted and contour interval is 2cm/sec. The wind blows between 0 day to 5 days and no forcing after that. The thick lines show propagate speeds.

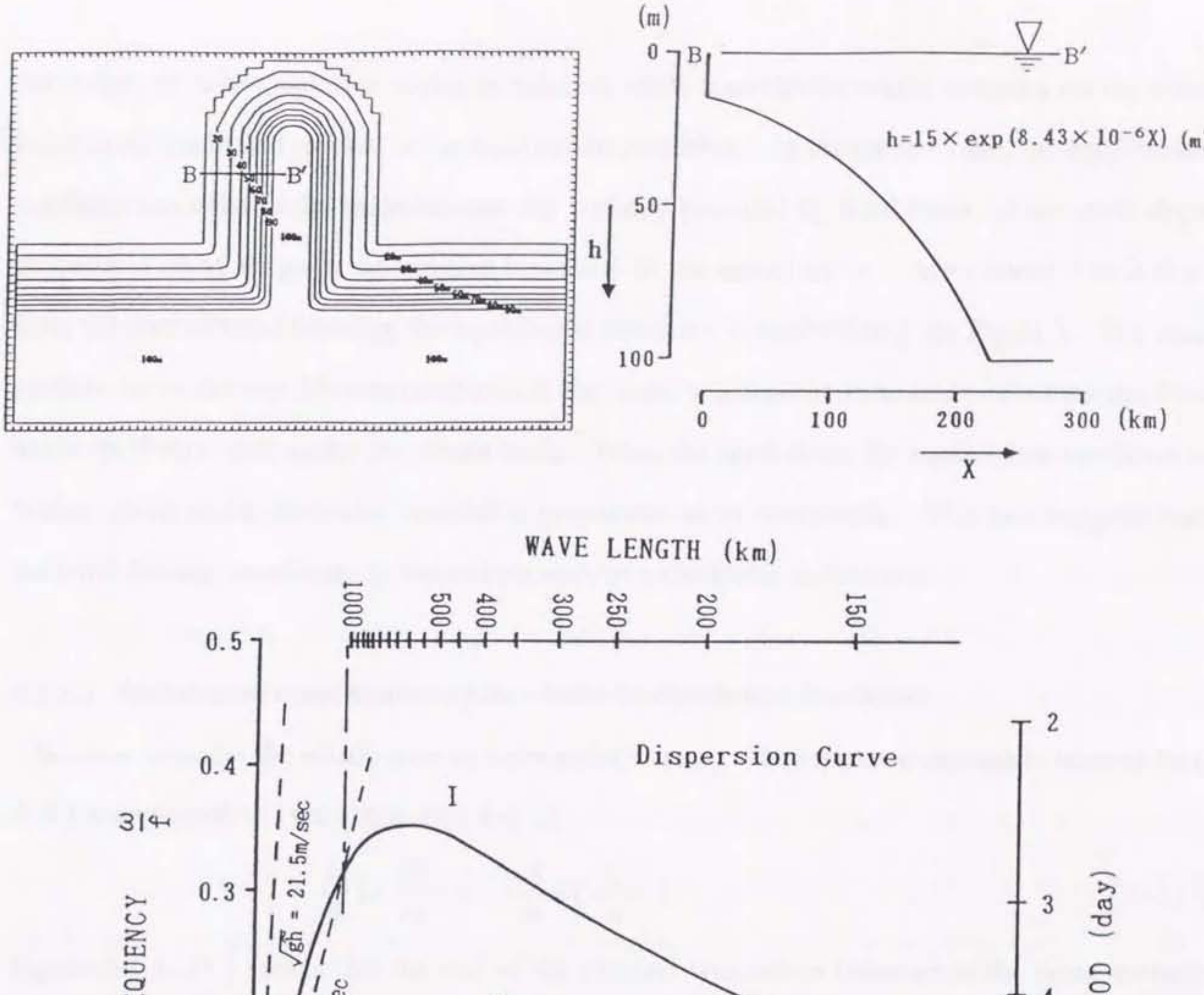

- $f = 8.34 \times 10^{-5}$ sec^{-1}
- $L = 225$ km
- $g = 9.8$ m/sec^2
- $\tilde{h} = 47.3$ m (mean depth of the section B-B′)

Fig.32 Dispersion curves for the lower three modes of shelf waves at line B–B′ (solid lines). Depth profile of the line B–B′ is denoted in the upper right–hand panel. Broken lines show propagation speeds and dash dot line shows the alongshore wavelength which corresponds to the first mode shelf wave.
ω:frequency, f:the Coriolis parameter, k:alongshore wavenumber, L:width of shelf.

After that, an anti-clockwise vortex is reduced, while a clockwise vortex evolutes on the shelf slope in the basin and reaches to the equilibrium condition. At the present case, the equilibrium condition can exist in the basin because the vorticity provided by wind stress on the shelf slope propagates away through the western boundary of the model basin. After about 2 or 3 days from the start of wind blowing, the equilibrium condition is established (see Fig.31). The time scale to be in the equilibrium condition is the same order as the time scale of which the first mode shelf wave propagates the whole basin. When the wind stops, the equilibrium condition is broken down and a clockwise circulation propagates away southward. This fact suggests that the wind forcing contributes to the maintenance of a clockwise circulation.

4.2.1.3 Maintenance mechanism of the clockwise circulation in a basin

We now consider the steady state of a clockwise vortex. Then the time dependent term of Eq.(4-9) is neglected and we obtain Eq.(4-11).

$$\frac{f}{h} U \frac{\partial h}{\partial x} = - \frac{\partial}{\partial x} \left(\frac{\tau_y}{h} \right) . \qquad (4\text{-}11)$$

Equation (4-11) means that the curl of the external wind force balances to the cross-isobath mass transport. In a case of the model basin, the equilibrium condition of a clockwise circulation with the structure of the first mode shelf wave is represented by Eq.(4-11) at the central part of the basin, i.e. the fluid particles move westward. In the northern part of the basin, since the wind forcing of x-direction is 0 m sec^{-1}, vorticity is not provided, i.e. the fluid particles can not move across the shelf slope. Thus, the fluid particles move eastward along the shelf slope, as the compensation transport of the cross-isobath transport at the central part of the basin. Therefore, a clockwise circulation stably exist in the basin during constant blowing of wind. On the other hand, in the western part of the basin, an anti-clockwise vortex dose not balance to the wind forcing, because fluid particles at southern part of this vortex can not move eastward due to the relation of Eq.(4-11). Therefore, an anti-clockwise circulation dose not evolute in this basin.

In the real Yellow Sea, the north-westerly winter wind is not steady but fluctuates. Hsueh and Pang (1989) suggested that the variability of current field in the Yellow Sea is also large according to the variation of wind forcing in winter. Next, we consider the case in which the wind forcing has periodical fluctuation, and the calculation results will be compared with the current observation results.

4.2.2 Periodical wind forcing with 4 days period

Figure 33 shows the time variations of the northward component of current velocity at mooring stations B, D and F shown by Hsueh and Tinsman (1991), using the observed data during January to April, 1986. In their paper, the wind vector was not shown. So, the northward components of wind vector at a Japan Meteorological Agency (JMA) Ocean Data Buoy in the East China Sea at the same period are also shown in this figure. The northward current occurs when the strong northerly wind blows and the southward current occurs when the weak northerly or southerly wind blows. Particularly, when the strong northerly wind blows after the weak northerly or southerly wind blows, the strong northward current occurs. The wind has periodical fluctuation for about 4 days period, and the currents of all three stations highly correlate with this periodical wind. Therefore, the case of periodical wind forcing with 4 days period is calculated with the use of the same model shown in Fig.28. The wind vector components of the x and y directions are given by

$$W_x = 0, \qquad (\mathrm{m\ sec^{-1}}), \qquad (4\text{–}12)$$

$$W_y = -5 + 5\cos(2\pi t / 4\mathrm{days}) \quad (\mathrm{m\ sec^{-1}}) \qquad (4\text{–}13)$$

respectively.

The calculation is carried out for 12 days (corresponds to 3 periods of the wind forcing). Figure 34 shows the time series of the y–component currents at points A to D which approximately, correspond to the observation stations of Hsueh and Tinsman (1991). The northward currents become strong when the northerly wind is maximum, and the southward currents become strong when the northerly wind become weak. These results qualitatively correspond to the observed one which is shown in Fig.33.

Figure 35 shows the sequential patterns of current vectors over one period of the wind forcing. When the northerly wind is maximum, an anti–clockwise and a clockwise vortices are generated

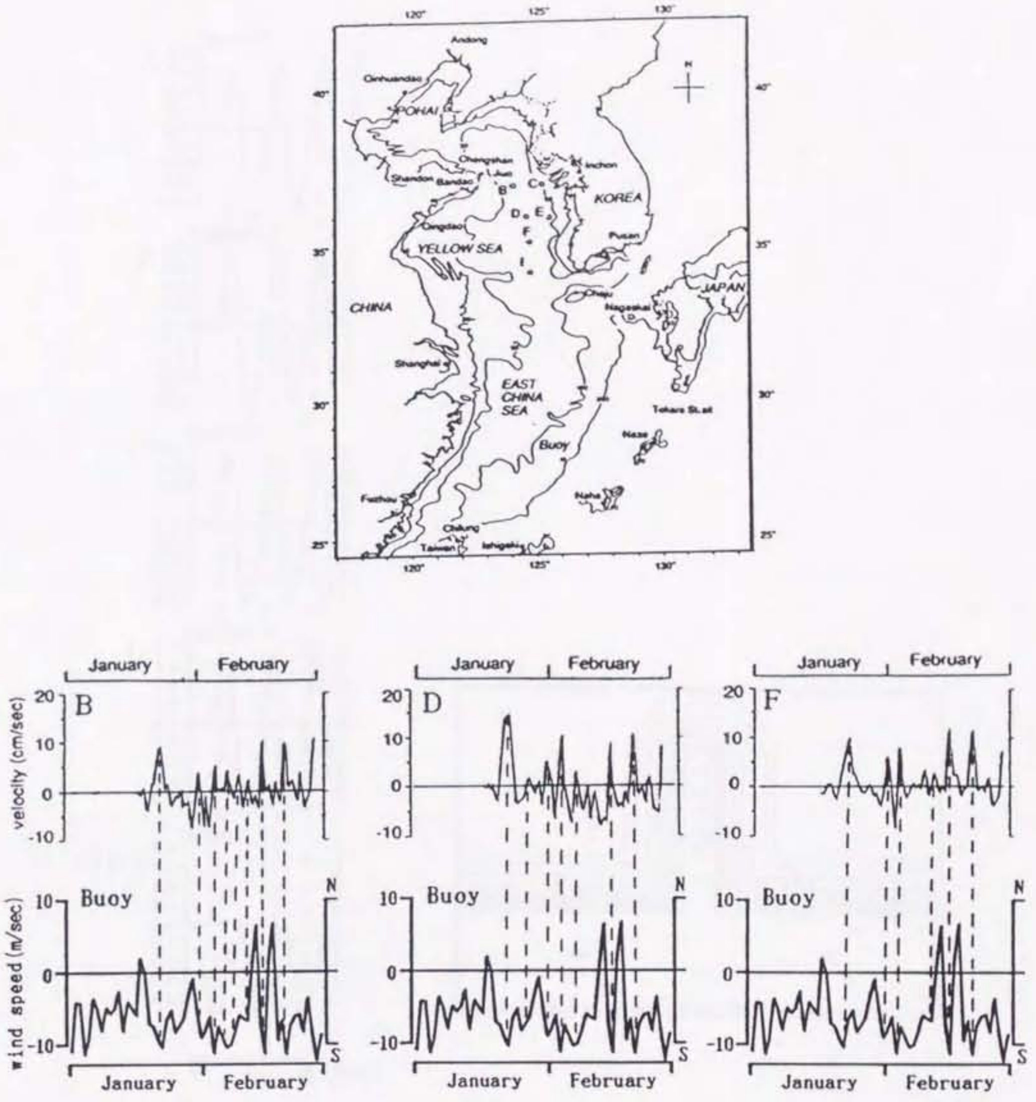

Fig.33 Map of the observation stations (upper panel) and time series of the northward component of the current velocity at mooring stations B, D and F during January–April 1986, by Hsueh and Tinsman (1991) and northward component of the same period wind velocity at a JMA Ocean Data Buoy. Broken lines show the time at northward current occurs.

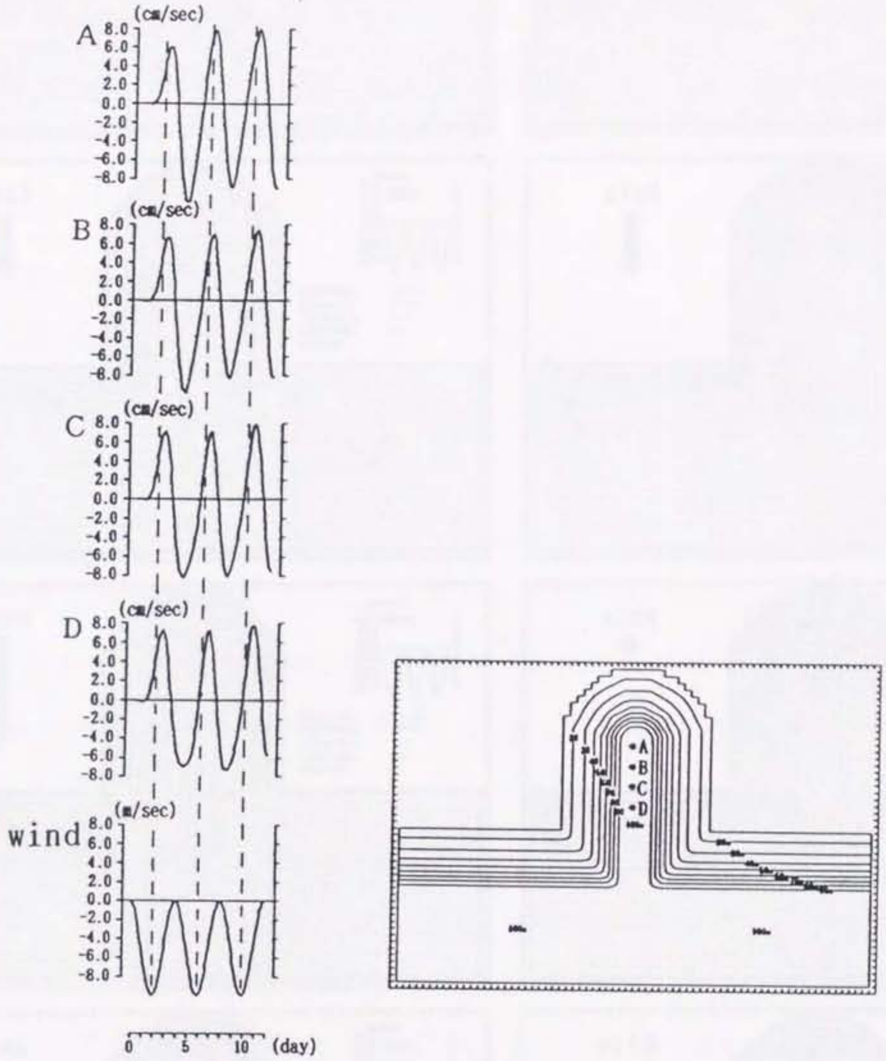

Fig.34 Time series of the y–axis component of the currents at points A,B,C,D of the right–hand panel and that of the wind forcing. Broken lines show the time at maximum northerly wind blows.

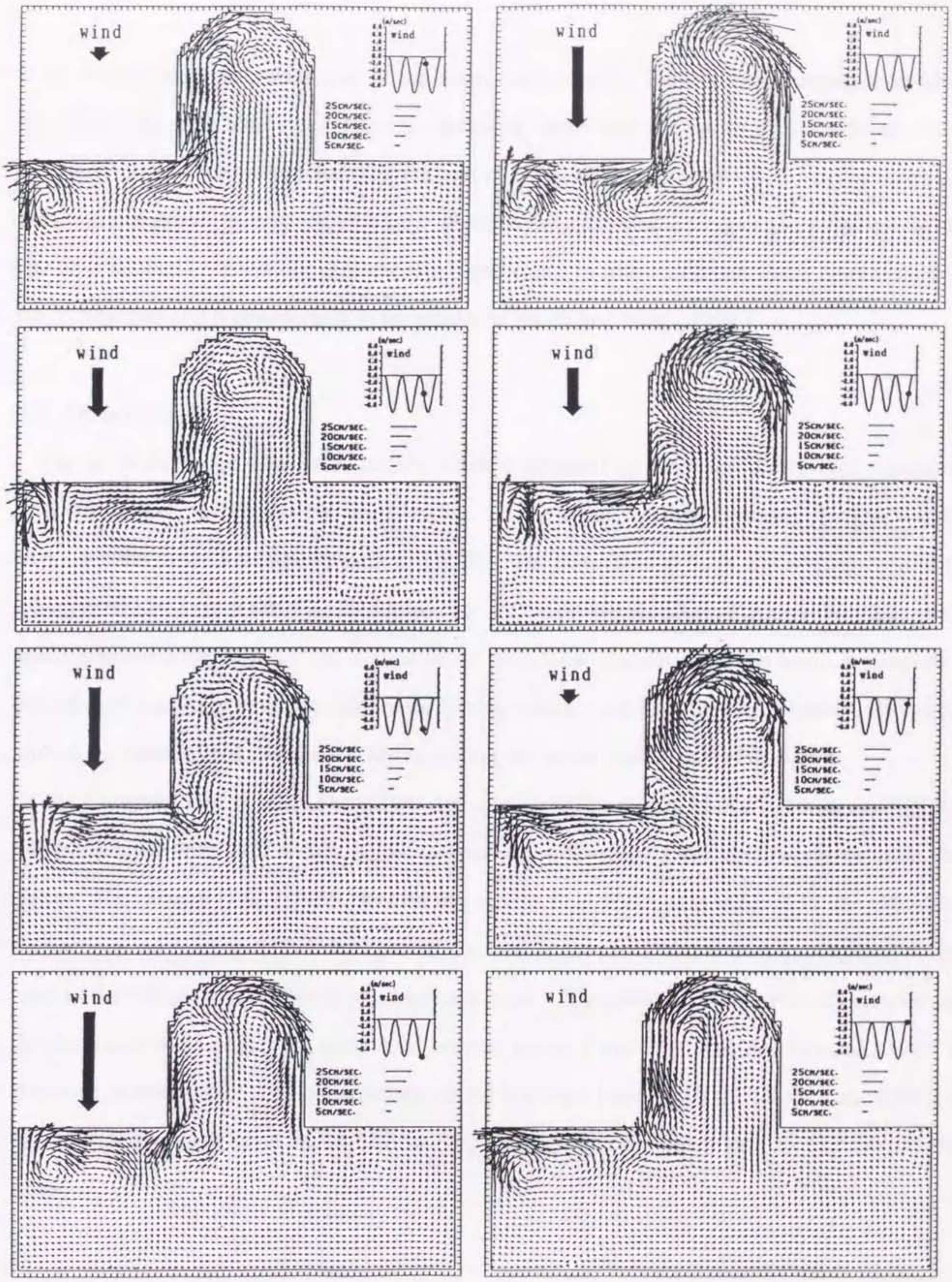

Fig.35 Time series of the current vectors over one period of the wind forcing. The north–westerly (negative–y direction) wind, which has average velocity (−5 m/sec), amplitude (5m/sec) and period (4 days), is blowing.

at the western and the eastern part of the basin, respectively. Both vortices propagate looking the coast to the right hand side. An anti-clockwise vortex dose not grow but a clockwise vortex becomes large and strong at the northern part of the basin. When the wind becomes weaker, both vortices propagate away southward. Namely, the shelf waves are generated and propagate one after another. This result expresses the significance of fluctuating part of the current field in the Yellow Sea and it corresponds to the results of Hsueh and Pang (1989).

4.3 Discussions

Figure 36 shows the circulation pattern which is obtained by averaging the current velocities over one period (4 days) of the wind forcing. In the basin, the time averaged circulation pattern is similar to the lower two panels of Fig.29. The time scale to be in equilibrium condition, which is obtained from dividing the basin scale, by the propagation speed of the first mode shelf wave is about 2 days. This fact means that a clockwise circulation in the basin is generated periodically according to the variable wind forcing with several days period. Namely, the steady part of the current field exists with the fluctuating one at the central part of the basin.

The clockwise vortex needs about 2 days to develop in this model. Such fact suggests that the northerly wind with over 4 days period is needed for developing the clockwise vortex in the Yellow Sea. Hsueh et al. (1986) treated the current field which was induced by the eventlike northerly wind forcing with 2 days period, i.e. before the clockwise vortex propagated to the head of the Yellow Sea, northerly wind became weak. Therefore, the clockwise vortex was not developed in their sequential pattern of current vector (see Fig.19 of Hsueh et al., 1986). However, in their mean circulation pattern during 120 days (see Fig.22 of Hsueh et al., 1986), a clockwise circulation exists in the Yellow Sea, although that is weaker than that of the present study.

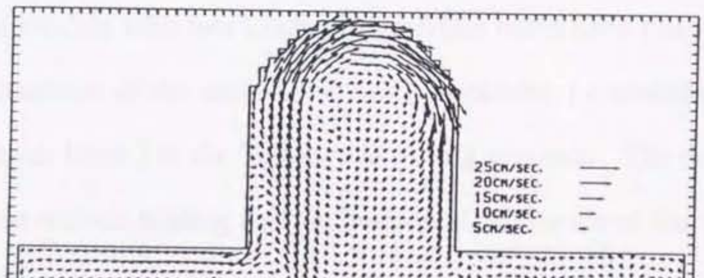

Fig.36 Circulation pattern obtained by averaging the current velocities over one wind period (4days)

5. Conclusion

The seasonal variation of the water circulations in the Yellow Sea and the East China Sea has been investigated with use of robust diagnostic numerical model experiments. The calculated results show that during summer an anti-clockwise circulation exists at the upper and middle layers but a clockwise one exists at the lower layer in the Yellow Sea. On the other hand, the calculated water circulation during winter shows different character from that during summer, i.e., a clockwise and an anti-clockwise circulation are developed from the surface to the bottom in the Yellow Sea and the East China Sea, respectively. The calculated water circulations during spring and autumn are similar to those in winter.

The numerical models with two kinds of simplified basin have been developed to examine the generation mechanisms of the anti-clockwise (clockwise) circulation at the upper and middle layers (at the lower layer) in the Yellow Sea during summer. The density distribution which is formed by the sea surface heating and the horizontal difference of the vertical mixing due to tidal current, drives the horizontal divergence at the upper and lower layers and the horizontal convergence at the middle layer. Accompanied by such horizontal divergence and convergence, a clockwise circulation is developed at the upper and lower layers and an anti-clockwise one at the middle layer. On the other hand, the density distribution which is formed by the sea surface heating and the topographic heat accumulation effect, drives the horizontal convergence in the upper layer and the horizontal divergence in the lower layer. Accompanied by such horizontal convergence and divergence, an anti-clockwise circulation is developed at the upper layer and a clockwise one at the lower layer. The circulation in the Yellow Sea during summer should be generated by these two effects which are mentioned above.

Furthermore, a simplified numerical model has been developed to examine the formation and variation mechanisms of a clockwise circulation in the Yellow Sea during winter. In the Yellow Sea, two vortices (an anti-clockwise vortex off Chinese coast and a clockwise vortex off Korean coast) are generated by the uniform north-westerly wind forcing during winter. Both vortices propagate looking the coast to its right hand side as the first mode shelf wave. An anti-clockwise circulation can not grow because it can not balance to the vorticity supplied by wind forcing. On the other hand, a clockwise circulation can grow at the northern part of the Yellow Sea and reaches to the equilibrium condition. Then the vorticity supplied by wind stress balances to the vorticity caused by stretching and shrinking of the water column. The time scale to reach the equilibrium condition, which is obtained from the propagation time of the first mode shelf wave from the mouth to the head of the Yellow Sea, is about 2 days. Therefore, the current field in the Yellow Sea highly fluctuates by responding to the variable wind with several days period, although such current field has the steady part.

Of course, there are some problems that are not examined exactly in this study. For example, in the case of summer, the horizontal heat flux between the East China Sea and the Yellow Sea was ignored, which may be expected to influence the circulations in the Yellow Sea during summer; In the case of spring, although weak southerly wind prevails, a clockwise circulation is developed from the surface to the bottom in the Yellow Sea. But the intensity of this circulation is much weaker than that of winter. It is expected that the effect of strong winter wind forcing remains in the spring density distribution of the Yellow Sea, i.e., the dynamics of a clockwise circulation in the Yellow Sea during spring can not be explained from that during winter. These problems will be investigated in the near future by including the effect of horizontal heat flux from the Kuroshio in summer and the effect of the water density distribution in spring.

The knowledge of the current field which is clarified in this paper will provide useful information to the investigation of the material cycling in the East China Sea and the Yellow Sea. Furthermore, the method of the diagnostic numerical experiment should be able to apply to the other marginal seas. It should be expected that only after the current fields of the all marginal seas in the world are understood, the study of the material cycling of carbon and other elements can be carried out quantitatively in the global scale.

Acknowledgments

The author wishes to express his sincere thanks to Prof.T.Yanagi, Prof.T.Kakinuma, Prof.M.Yamaguchi and Dr.H.Takeoka of Ehime University for their discussions, suggestions and encouragements. He also expresses many thanks to Dr.Y.Isoda of Hokkaido University and Mr.H.Akiyama of Ehime University for their fruitful discussions. The author much indebted to Prof.M.Kubota of Tokai University for his kind providing COADS and to Japan Meteorological Agency for kindly supplying the wind data at the East China Sea buoy station. The numerical experiments were carried out on a FACOM M−770 of the Computer Center of Ehime University.

References

Backhaus, J.O. (1983) : A semi-implicit scheme for the shallow water equation for application to shelf water sea modeling. Continental Shelf Res., 2, 243-254.

Choi,B.H. (1984) : A three-dimensional model of the East China Sea. *In* " Ocean Hydrodynamics of Japan and East China Seas ", *ed. by* T.Ichiye, Elsevier, Amsterdum, 209-224.

Choi,B.H. and H.J.Lie (1992) : Physical oceanography program of the East China Sea and the East Sea (Japan Sea) dynamics in Korea. Proceeding of PORSEC-92, 1-28.

Fang,G., B.Zhao and Y.Zhu (1991) : Water volume transport through the Taiwan strait and the continental shelf of the East China Sea measured with current meters. *In* " Oceanography of Asian Marginal Seas ", *ed. by* K.Takano, Elsevier, Amsterdum, 345-358.

Fukase,S. (1975) : Bottom water on the continental shelf in the East China Sea. Umi to Sora (Sea and Sky) , 51, 13-15. (in Japanese)

Fujio,S. and N.Imasato (1991) : Diagnostic calculation for circulation and water mass movement in the deep Pacific. J.Geophys, Res., 96, 759-774.

Hsueh,Y., R.D.Romea and P.W.de Witt (1986) : Wintertime winds and coastal sea-level fluctuations in the northeast China Sea. Part II : Numerical Model. J.Phys.Oceanogr., 16, 241-261.

Hsueh,Y. and I.C.Pang (1989) : Coastally trapped long waves in the Yellow Sea. Phys.Oceanogr., 19, 612-625.

Hsueh,Y. and J.H.Tinsman,III (1991) : Synoptic band wintertime heat exchanges in the Yellow Sea. *In* " Oceanography of Asian Marginal Seas", Ed. by K.Takano, Elsevier, Amsterdam, 269-276.

Ishii,T. and J.Kondo (1987) : Seasonal variation of the heat balance of the East China Sea. Tenki (Weather), 34, 8, 517-526. (in Japanese)

Ishii,T. and J.Kondo (1993) : Seasonal variation of the heat balance in the East China Sea and its vicinity — Ocean heat transport and Ocean storage of heat —. Tenki (Weather), 40, 5, 309–324. (in Japanese)

Japan Oceanographic Data Center (1978) : Marine environmental atlas – northwestern Pacific Ocean II. 157p.

Niino,H. and K.O.Emery (1961) : Sediments of shallow portions of East China Sea and South China Sea. Geological Society of America Bulletin, 72, 731–762.

James,I.D. (1977) : A model of the annual cycle of temperature in the frontal region of the Celtic Sea. Estuarine, Coastal Marine Sci., 5, 339–353.

Kondo,M. (1985) : Oceanographic investigations of fishing ground in the East China Sea and the Yellow Sea – I. Characteristics of the mean temperature and salinity distributions measured at 50m and near the bottom. Bulletin of Seikai Regional Fisheries Research Laboratory, 62, 19–66. (in Japanese)

Na,J.Y., J.W.Seo and S.K.Han (1992) : Monthly–mean sea surface winds over the adjacent seas of Korea Peninsula. J.Oceanogr.Soc.Korea, 27, 1–10.

Ohshima,K. and H.Miyake (1990) : A numerical study of wind–induced circulation off southern coast of Hokkaido and in Funka Bay. Umi to Sora (Sea and Sky), 66, 53–66. (in Japanese)

Oonishi,Y. (1975) : Development of the current induced by the topographic heat accumulation (I) — The case of the axisymmetric basin —. J.Oceanogr.Soc.Japan, 31, 243–254.

Qiu,B. and N.Imasato (1990) : A numerical study on the formation of the Kuroshio countercurrent and the Kuroshio branch current in the East China Sea. Continental Shelf Res., 10, 165–184.

Sarmiento,J.L. and K.Bryan (1982) : An ocean transport model for the North Atlantic. J.Geophys.Res., 87, 394–408.

Takeoka,T., Y.Ohno and N.Inahata (1991) : Roles of horizontal processes in the formation of density stratification in Hiuchi-Nada. J.Oceanogr.Soc.Japan, 47, 33-44.

Tawara,S. and T.Yamagata (1991) : Seasonal formation of bottom water in the Yellow Sea and its interannual variability. Umi to Sora (Sea and Sky), 66, 273-282. (in Japanese)

Wadachi,K. *ed.* (1987) : Encyclopedia of Oceanography. Tokyodo-Press, Tokyo, 589pp.

Woodruff,S.D., R.J.Slutz, R.L.Jenne and P.M.Steurer (1987) : A comprehensive Ocean-Atmosphere Data Set., Bulletin American Meteorological Society, 68, 1239-1250.

List of Tables

List of Figures

Fig.32 Dispersion curves for the lower three modes of shelf waves at line B–B' (solid lines). Depth profile of the line B–B' is denoted in the upper right–hand panel. Broken lines show propagation speeds and dash dot line shows the alongshore wavelength which corresponds to the first mode shelf wave. ω:frequency, f:the Coriolis parameter, k:alongshore wavenumber, L:width of shelf.

Fig.33 Map of the observation stations (upper panel) and time series of the northward component of the current velocity at mooring stations B, D and F during January–April 1986, by Hsueh and Tinsman (1991) and northward component of the same period wind velocity at a JMA Ocean Data Buoy. Broken lines show the time at northward current occurs.

Fig.34 Time series of the y–axis component of the currents at points A,B,C,D of the right–hand panel and that of the wind forcing. Broken lines show the time at maximum northerly wind blows.

Fig.35 Time series of the current vectors over one period of the wind forcing. The north–westerly (negative–y direction) wind, which has average velocity (-5 m sec^{-1}), amplitude (5m sec^{-1}) and period (4 days), is blowing.

Fig.36 Circulation pattern obtained by averaging the current velocities over one wind period (4 days).